Chemical Science

ROYAL SOCIETY OF CHEMISTRY

EDGE ARTICLE

View Article Online
View Journal | View Issue

Check for updates

Cite this: *Chem. Sci.*, 2026, **17**, 1073

All publication charges for this article have been paid for by the Royal Society of Chemistry

Open Access Article. Published on 03 November 2025. Downloaded on 4/1/2026 3:19:42 PM. This article is licensed under a Creative Commons Attribution-NonCommercial 3.0 Unported Licence.

Magneto-voltaic activity of single-atom iron on reduced graphene oxide for magneto-catalytic conversion of H_2O_2 into O_2

Chieh-Wei Chung,†[a] Jyun-Yau Huang,†[b] Jing-Guan Liang,†[ac] Linda Iffland,[de] Loise Ann Dayao,[a] Dinesh Kumar Dhanthala Chittibabu,[f] Chong-Chi Chi,[c] Jeng-Lung Chen,[g] Ting-Shan Chan,[g] Chi-Liang Chen,[g] Ying-Rui Lu,[g] Chieh-Cheng Huang,[a] Ho-Hsiu Chou,[h] Zong-Hong Lin,[i] Ying-Chieh Chen,[c] Ming-Yen Lu,[c] Hsin-Tsung Chen,*[f] Ulf-Peter Apfel,*[de] Yei-Chen Lai*[j] and Tsai-Te Lu*[abf]

Recent advances in magnetically enhanced (electro)catalysis have disclosed the potential of magnetic fields to modulate reaction kinetics and catalytic performance. Herein, a combination of alternating magnetic field (AMF) as a physical stimulus, reduced graphene oxide (rGO) as a magneto-sensitizer, single-atom Fe on rGO (FeSA:rGO) as the catalytic active site, and H_2O_2 as a dual reductant and oxidant demonstrated a proof-of-concept magneto-catalytic process that is thermodynamically driven solely by magneto-voltaic activity. Upon application of an AMF to electroconductive FeSA:rGO, AMF-induced charge separation led to formation of low-lying electron holes (E_{HOMO} = 2.41/2.43 eV) and excited electrons (E_{LUMO} = −0.65/−0.57 eV), which triggered AMF power-dependent magneto-voltaic and magneto-electric activity (0.19–1.56 V and 0.15–0.62 mA). In the presence of H_2O_2, these AMF-induced low-lying electron holes in FeSA:rGO promoted oxidation of the Fe^{3+} resting state leading to transient formation of a high-valent Fe^{4+} species, which served as a critical intermediate for magneto-catalytic oxidation of H_2O_2 and evolution of O_2. Furthermore, a kinetic study unveiled that FeSA:rGO concentration, H_2O_2 concentration, and AMF power played key roles in controlling the rates for FeSA:rGO-mediated magneto-catalytic oxygen evolution reaction. Consequently, these investigations established a mechanistic foundation for the future development of magneto-catalytic systems by integrating AMF-responsive magneto-sensitizers with diverse catalytic active sites.

Received 16th July 2025
Accepted 29th October 2025

DOI: 10.1039/d5sc05275k

rsc.li/chemical-science

Introduction

In 2011, Pt_1/FeO_x, consisting of well-dispersed single Pt atoms decorated on the surfaces of iron oxide nanocrystallites, was reported as the first single atom catalyst (SAC) for CO oxidation.[1] By virtue of inheriting advantages from homogeneous catalysts and natural metalloenzymes, SACs have emerged as promising heterogeneous catalysts featuring (a) well-dispersed metal active sites with a well-defined coordination environment, (b) superior catalytic activity/selectivity tailored by the coordination geometry of the metal active sites, and (c) utmost atomic utilization efficiency.[2–6] For preparation of Fe-based SACs, multifarious synthetic strategies including high-temperature pyrolysis,[7–10] mass-selected soft landing,[11,12] ball milling,[13,14] and dangling bond trapping were reported and summarized in SI Table 1.[15,16] In addition to the single-atom metal active sites, the synergistic structural and electronic effects of the supporting materials in SACs play a critical role in optimizing and strengthening their applications in (electro-/photo-)catalysis, artificial nanozymes, energy storage/

[a]*Institute of Biomedical Engineering, National Tsing Hua University, Hsinchu, 30013, Taiwan. E-mail: ttlu@mx.nthu.edu.tw*

[b]*Department of Chemistry, National Tsing Hua University, Hsinchu, 30013, Taiwan*

[c]*Department of Materials Science and Engineering, National Tsing Hua University, Hsinchu, 30013, Taiwan*

[d]*Department of Chemistry and Biochemistry, Activation of Small Molecules/Technical Electrochemistry, Ruhr-Universität Bochum, 44801 Bochum, Germany*

[e]*Department of Electrosynthesis, Fraunhofer UMSICHT, 46047 Oberhausen, Germany. E-mail: ulf.apfel@rub.de*

[f]*Department of Chemistry, Chung Yuan Christian University, Taoyuan, 32023, Taiwan. E-mail: htchen@cycu.edu.tw*

[g]*National Synchrotron Radiation Research Center, Hsinchu, 30076, Taiwan*

[h]*Department of Chemical Engineering, National Tsing Hua University, Hsinchu, 30013, Taiwan*

[i]*Department of Biomedical Engineering, National Taiwan University, Taipei, 106319, Taiwan*

[j]*Department of Chemistry, National Chung Hsing University, Taichung, 402202, Taiwan. E-mail: yeichenlai@nchu.edu.tw*

† These authors contributed equally: Dr Chieh-Wei Chung, Mr Jyun-Yau Huang, and Mr Jing-Guan Liang.

© 2026 The Author(s). Published by the Royal Society of Chemistry

Open Access Article. Published on 03 November 2025. Downloaded on 4/1/2026 3:19:42 PM. This article is licensed under a Creative Commons Attribution-NonCommercial 3.0 Unported Licence.

conversion, biosensors, and biomedicine.[3–5,7–12,17–25] In particular, during electrocatalytic reduction of dioxygen promoted by *pf*SAC-Fe, the electroconductive graphene supporting material provided an electron-transfer pathway to the single-atom Fe active site for superior catalytic oxygen reduction reaction.[11] Besides, for the FePc/hollow nitrogen-doped carbon nanosphere (HNCS) nanozyme featuring a strong π-electron conjugation, near-infrared irradiation induced a photothermal effect of the HNCS supporting material, which enhanced the activation of H_2O_2 by the single-atom Fe active site on the conjugated FePc.[25]

Recently, external application of an alternating magnetic field (AMF) was reported to enhance a variety of metal-mediated (electro)catalytic reactions due to the magnetic heating (increase of local apparent temperature at the (electro)catalyst through Brownian/Néel relaxations of magneto-sensitizers),[26–35] magnetohydrodynamic (improvement of diffusion for reactants/electrolytes by Lorentz force),[30,35,36] and spin polarization effects.[27,30,35,37–40] In the AMF-enhanced electrocatalytic oxidation of H_2O leading to evolution of O_2, particularly, (1) spin conservation of unpaired electrons in the π* orbital of the O_2 moiety in the lattice oxygen oxidation mechanism and (2) spin-selective electron removal from σ_{M-O} and σ_{O-H} bonds in the M–OOH intermediate in the adsorbate evolution mechanism were reported to lower the kinetic barrier for transformation of singlet precursors/intermediates (*i.e.* M–OH/M=O/M–OOH) into triplet O_2.[37–39] On the other hand, based on Lenz's law, application of an AMF to electrically conductive materials induced generation of electric currents (*i.e.* eddy currents), of which the intensity was proportional to the electrical conductivity of materials as quantified by Faraday's law.[32,41] Despite the reported generation of electric currents in electrically conductive materials under AMF, however, the magneto-voltaic properties of these materials and unexplored utilization of magneto-voltaic activity as a solely thermodynamic driving force to magneto-catalysis remained elusive.

In traditional radiotherapy (RT) and photodynamic therapy (PDT), O_2 plays a critical role in the generation of reactive oxygen species (*i.e.* O_2^- or $^1O_2$) leading to DNA damage and inducing cancer cell apoptosis.[42–44] Due to the rapid growth and metabolic demands of solid tumors, however, hypoxia (≤2% O_2) appears as one of the distinctive features within the tumor microenvironment (TME).[45–47] Moreover, anaerobic glycolysis and mitochondrial dysfunction under this hypoxic TME induce excessive production of hydrogen peroxide (H_2O_2) as a byproduct, of which concentration in the TME can be increased to ~100 μM higher than that at ~1–70 nM under normal intracellular conditions.[48–51] Taking advantage of endogenous H_2O_2, MnO_2-based nanomaterials were widely reported for catalytic conversion of H_2O_2 into O_2 reversing the hypoxic TME and enhancing anti-cancer RT/PDT.[52,53] In addition to MnO_2-mediated oxygen evolution reaction (OER) from H_2O_2, amorphous iron nanoparticles, ferrous phosphide nanorods, and iron-engineered silica frameworks were also found to promote production of highly cytotoxic hydroxyl radicals (˙OH) from Fenton reaction of H_2O_2 and to induce tumor cell death.[54–56] Of interest, a dual enzyme-mimicking nanocomposite, single-atom Fe on *N*-doped mesoporous carbon nanospheres (SAFe-NMCNs), highlighted the synergistic anti-cancer effects derived from concomitant generation of O_2 and ˙OH in the TME.[57] Under NIR-II irradiation, the single-atom Fe–N_4 active site initiates production of cytotoxic ˙OH through peroxidase (POD)-like activity and evolution of O_2 through catalase (CAT)-like activity, thereby enhancing the photothermal anti-cancer treatment in a synergistic manner. Despite these insights from nanozyme-based cancer therapy, the focus on cancer eradication often overshadows the critical need for post-cancer treatment, namely, the need for the repair and regeneration of damaged surrounding tissue potentially *via* electrical stimulation.[58,59]

Inspired by the potential of AMF-induced electric current, magneto-voltaic activity, and magneto-catalysis, herein, the reaction of GO with Fe-precursor complexes followed by reduction of GO was explored as a pyrolysis-free approach to prepare single-atom Fe on reduced GO (FeSA:rGO, Scheme 1a). Under the external application of AMF to FeSA:rGO, the electrically conductive rGO served as a magneto-sensitizer to trigger AMF-induced electric current and magneto-voltaic activity (Scheme 1b). For the first time, the intensity of AMF-induced magneto-voltaic activity was measured and discovered to be dependent on AMF power. Considering the elevated production of H_2O_2 under the hypoxic TME, H_2O_2 was chosen as a dual reductant and oxidant to demonstrate the proof-of-concept magneto-catalytic transformation of H_2O_2 into O_2 promoted by FeSA:rGO under an AMF (Scheme 1b). The magneto-voltaic activity and magneto-catalytic nature of FeSA:rGO revealed its potential to reverse the hypoxic TME, to trigger anti-cancer activity, and to potentially induce magneto-electric stimulation on tissue repair, which requires an investigation in the near future.

Results and discussion

Characterization of single-atom Fe on graphene oxide (FeSA:GO)

Details for the reactivity study of GO toward Fe complex [Na-18-crown-6-ether][$(NO)_2Fe(\eta^2\text{-}BH_4)$] (**DNIC-BH4**, or complex [$(NO)_2$Fe(TMEDA)] (**DNIC-TMEDA**)) leading to the formation of Fe:GO (or Fe(TMEDA):GO) were discussed in the Methods. As shown in SI Fig. 5a, Fe:GO and Fe(TMEDA):GO exhibited PXRD peaks at $2\theta = 9.3°$ and 9.1°, respectively, which corresponded to the (001) plane of GO. These PXRD features, which were consistent with that of GO, indicated retained crystalline structure of GO after immobilization of Fe. Moreover, (HR)TEM images of GO, Fe:GO, and Fe(TMEDA):GO supported the two-dimensional sheet-like morphology of GO before and after modification (Fig. 1a and b and SI Fig. 6). Of importance, no apparent aggregation of Fe nanoparticles was observed on the flat and unspotted surface of Fe:GO and Fe(TMEDA):GO. Upon utilization of HAADF-STEM, atomic dispersion of Fe single atoms anchoring on a GO substrate was identified as apparent bright dots in the HAADF-STEM images of Fe:GO and Fe(TMEDA):GO. As shown in SI Fig. 7, the intensity profile analysis of Fe:GO and Fe(TMEDA):GO determined the shortest distances

© 2026 The Author(s). Published by the Royal Society of Chemistry

Open Access Article. Published on 03 November 2025. Downloaded on 4/1/2026 3:19:42 PM.
This article is licensed under a Creative Commons Attribution-NonCommercial 3.0 Unported Licence.

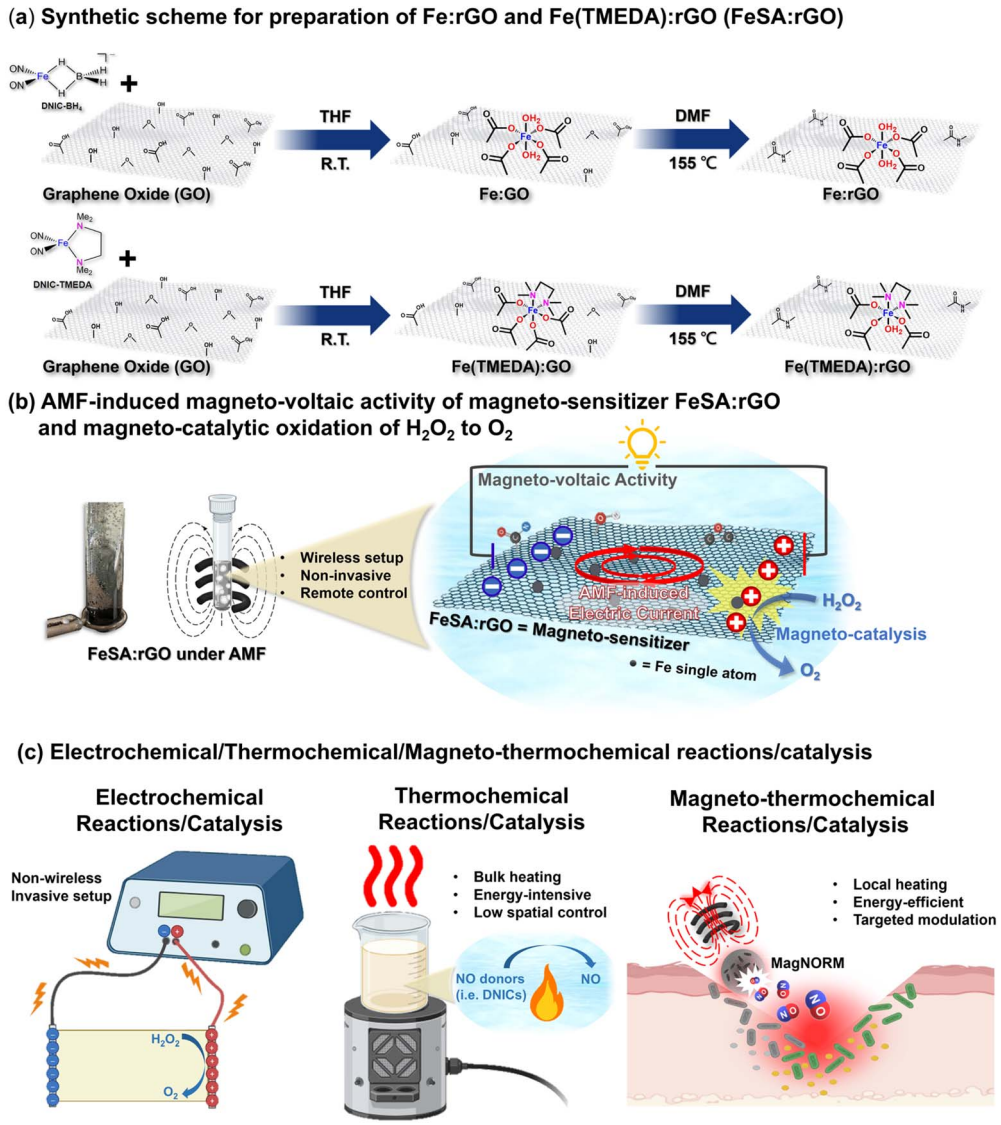

Scheme 1 Schematic illustration for (a) preparation of FeSA:rGO through reaction of Fe precursor complexes with GO followed by solvothermal reduction of FeSA:GO to FeSA:rGO, (b) AMF-induced magneto-voltaic activity of magneto-sensitizer FeSA:rGO and magneto-catalytic oxidation of H_2O_2 to O_2 explored in this study, and (c) conceptual comparisons with electrochemical catalysis (*i.e.* oxidation of H_2O_2 to O_2), thermochemical reactions (*i.e.* heat-induced release of NO from NO donors), and magneto–thermochemical reactions (*i.e.* magnetic responsive release of NO from MagNORM).

between adjacent Fe atoms to be 4.7–6.5 Å in Fe:GO and 4.4–5.3 Å in Fe(TMEDA):GO. These analyses provide additional support for the well-dispersed nature of single-atom Fe centers on GO and exclude the agglomeration of Fe atoms.[60] Accordingly, Fe:GO and Fe(TMEDA):GO were best described as a two-dimensional sheet-like GO decorated with well-dispersed single-atom Fe centers. In addition, detailed discussions on XPS study of GO, Fe:GO, and Fe(TMEDA):GO were included in the Methods.

Mössbauer and XANES in combination with EXAFS analyses were further performed to elucidate the electronic structure and local coordination environment of single-atom Fe sites in both Fe:GO and Fe(TMEDA):GO. As shown in Fig. 1c, deconvolution of the major doublet feature observed in the Mössbauer spectrum of Fe:GO required a two-site fitting. Based on the two-site fitting, the isomer shift (δ) of 0.59 mm s^{-1} with a quadrupole doublet (ΔE_Q) of 0.47 mm s^{-1} for site #1 (65.6%) and the isomer shift (δ) of 0.47 mm s^{-1} with a quadrupole doublet (ΔE_Q) of 0.43 mm s^{-1} for site #2 (27.9%) were consistent with the high-spin Fe^{3+} center with O-/N-based ligands.[61] The minor site #3 (6.5%) featuring an isomer shift (δ) of 1.35 mm s^{-1} with a quadrupole doublet (ΔE_Q) of 2.04 mm s^{-1} may suggest minimal presence of a high-spin Fe^{2+} center with O-/N-based ligands in the Fe:GO.[61] In Fe(TMEDA):GO, formation of the high-spin Fe^{3+} center with O-/N-based ligands was evidenced by comparable Mössbauer parameters (Fig. 1d), namely, an isomer shift (δ) of 0.55 mm s^{-1} with a quadrupole doublet (ΔE_Q) of 0.44 mm s^{-1} for site #1 (50.9%) and isomer shift (δ) of 0.55 mm s^{-1}

Open Access Article. Published on 03 November 2025. Downloaded on 4/1/2026 3:19:42 PM.
This article is licensed under a Creative Commons Attribution-NonCommercial 3.0 Unported Licence.

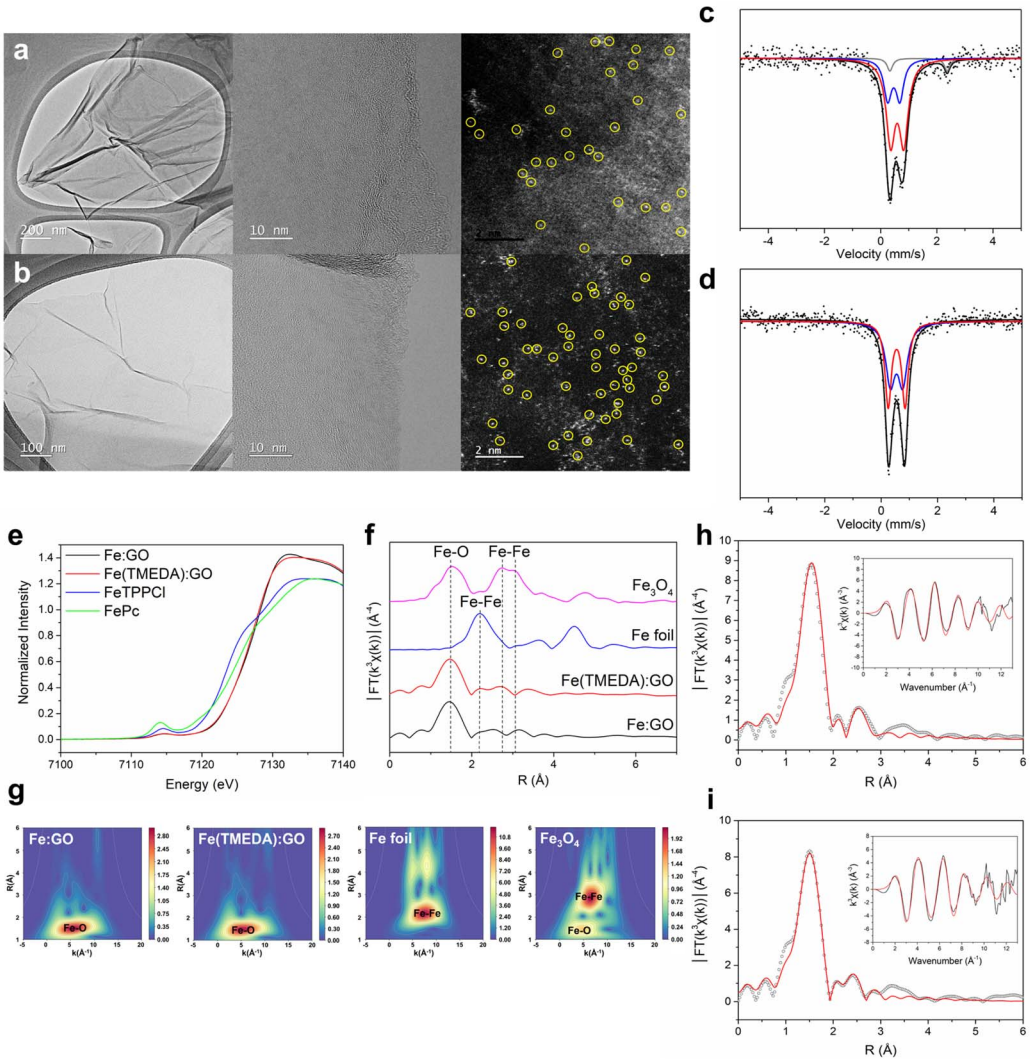

Fig. 1 Characterization of single-atom Fe on GO (FeSA:GO). (a and b) TEM, HRTEM, and HAADF-STEM images of (a) Fe:GO and (b) Fe(TMEDA):GO. The Fe single atoms were highlighted with yellow circles. (c and d) Mössbauer spectra of (c) Fe:GO and (d) Fe(TMEDA):GO collected at 80 K (square dot), whereas the different Fe sites were fitted in red, blue, and gray. (e) Normalized Fe K-edge XANES spectra of FePc, Fe(TPP)Cl, Fe:GO, and Fe(TMEDA):GO. (f) Fourier-transformed magnitudes of the experimental Fe K-edge EXAFS signals of Fe:GO, Fe(TMEDA):GO, Fe foil, and Fe_3O_4. (g) Wavelet transforms of k^3-weighted Fe K-edge EXAFS for Fe:GO, Fe(TMEDA):GO, Fe foil, and Fe_3O_4. (h and i) Phase-shift-corrected Fourier transforms (and EXAFS data, inset) and the best fits (red) of (h) Fe:GO and (i) Fe(TMEDA):GO.

with a quadrupole doublet (ΔE_Q) of 0.60 mm s^{-1} for site #2 (49.1%). On the other hand, these Mössbauer features displayed by both Fe:GO and Fe(TMEDA):GO were distinctive from those exhibited by Fe_3O_4 and zero-valence Fe nanoparticles (SI Fig. 8), which provided additional support to exclude aggregation of Fe nanoparticles during the GO-induced transformation of **DNIC-BH4** and **DNIC-TMEDA**.

Fourier-transformed magnitudes and wavelet transform (WT) plots for the experimental Fe K-edge EXAFS signals of Fe:GO, Fe(TMEDA):GO, Fe foil, and Fe_3O_4 are depicted in Fig. 1f and g, whereas discussions on Fe K-edge XANES spectra for these materials (Fig. 1e) are described in Methods. Accordingly, Fe:GO and Fe(TMEDA):GO displayed the first-coordination shell of Fe–O scattering paths at $R = 1.53$ Å/$k = 5.4$ $Å^{-1}$ and $R = 1.50$ Å/$k = 5.4$ $Å^{-1}$, respectively, which were similar to that at $R = 1.50$ Å/$k = 5.0$ $Å^{-1}$ featuring Fe_3O_4. Moreover, as opposed to the Fe–Fe scattering paths at $R = 2.2$ Å/$k = 7.5$ $Å^{-1}$ and $R = 2.7$–3.1 Å/$k = 6.5$ $Å^{-1}$ exhibited by Fe foil and Fe_3O_4, respectively, the absence of formation of distinctive/strong Fe–Fe scattering in Fe:GO and Fe(TMEDA):GO echoed the buildup of well-dispersed single-atom Fe on the carbonaceous matrix.

To further gain insight into the local coordination environment of single-atom Fe sites, the best fits to Fourier transforms and EXAFS data of Fe:GO and Fe(TMEDA):GO were collected in Fig. 1h–i and Table 1, whereas the detailed fitting process was collected in SI Tables 2 and 3. In the best fit of Fe:GO, a 2.01 Å Fe–O single scattering path was designated as the first-shell feature with a coordination number of six. In addition, inclusion of an Fe–C single scattering path at 3.06 Å and a corresponding Fe–O–C obtuse triangle at 3.39 Å resulted in

© 2026 The Author(s). Published by the Royal Society of Chemistry

Open Access Article. Published on 03 November 2025. Downloaded on 4/1/2026 3:19:42 PM. This article is licensed under a Creative Commons Attribution-NonCommercial 3.0 Unported Licence.

Table 1 Best-fit parameters to EXAFS data of FeSA:GO and FeSA:rGO[a]

Scattering path	N^a	R (Å)[a]	σ^2 (Å^2)[a]
Fe:GO			
Fe–O	6	2.01	0.007
Fe–C_1[a]	4	3.06	0.007
Fe–O–C_1[a]	4	3.39	0.006
Fe(TMEDA):GO			
Fe–N	2	2.16	0.010
Fe–O	4	1.99	0.006
Fe–C_T[a]	2	2.54	0.020
Fe–C_1[a]	4	2.93	0.012
Fe:rGO			
Fe–O	6	2.01	0.008
Fe–C_1[a]	4	3.04	0.009
Fe–O–C_1[a]	4	3.39	0.002
Fe(TMEDA):rGO			
Fe–N	2	2.20	0.004
Fe–O	4	1.98	0.005
Fe-C_T[a]	2	2.99	0.002
Fe–C_1[a]	3	3.39	0.003
Fe–O–C_1[a]	3	3.47	0.003

[a] k range = 2.5–10.8 Å^{-1} for Fe:GO, 2.6–10.9 Å^{-1} for Fe(TMEDA):GO, 2.6–10.9 Å for Fe:rGO, and 2.5–8.8 Å for Fe(TMEDA):rGO. N = coordination number. R = distance. σ^2 = Debye–Waller factor. C_1 = monodentate carboxylate. C_T = bidentate tetramethylenediamine.

a significant improvement of fit to the second-shell feature within the range of 1.0–3.0 Å, which was assigned to four monodentate carboxylate ligands derived from GO. That is, the local coordination environment of the single-atom Fe site in Fe:GO was best described as $[Fe^{3+}(L)_2(\eta^1\text{-O-GO}_{carboxylate})_4]^{n-}$ (L = H_2O or OH^-). For Fe(TMEDA):GO, in addition to the 2.16 Å Fe–N single scattering path (coordination number = 2) derived from chelation of TMEDA, the first-shell feature of Fe(TMEDA):GO was best fitted with an additional 1.99 Å Fe–O single scattering path with a coordination number of four, namely an octahedral local geometry of the single-atom Fe center. Similar to Fe:GO, coordination of four monodentate GO-carboxylate ligands to the single-atom Fe site in Fe(TMEDA):GO was evidenced by the Fe–C single scattering path at 2.93 Å. Based on the fitting to Fe(TMEDA):GO within the range of 1.0–3.0 Å, of importance, the reaction of GO with **DNIC-TMEDA**, in comparison with **DNIC-BH4**, resulted in the substitution of two monodentate L by the bidentate TMEDA ligand yielding the $[Fe^{3+}(TMEDA)(\eta^1\text{-O-GO}_{carboxylate})_4]^{n-}$ center in Fe(TMEDA):GO.

According to the comprehensive characterization of Fe:GO/Fe(TMEDA):GO together with the parallel reactivity study of **DNIC-BH4**/**DNIC-TMEDA** toward benzoic acid/phenol/styrene oxide (see Methods for details), proposed mechanisms for GO-induced conversion of **DNIC-BH4**/**DNIC-TMEDA** and impregnation of a well-dispersed single-atom Fe site in Fe:GO/Fe(TMEDA):GO were discussed below. During the reaction of GO and **DNIC-BH4**, deprotonation of the carboxylic acid ($pK_a = 4.1$)/phenol (pK_a = 9.3) groups of GO by $[BH_4]^-$ in **DNIC-BH4** resulted in evolution of $H_{2(g)}$ and coordination of $GO_{carboxylate}$/$GO_{phenoxide}$ to the transient DNIU $[Fe(NO)_2]$ leading to formation of proposed intermediate $[(NO)_2Fe(GO_{carboxylate})_x\text{-}(GO_{phenoxide})_y]^{n-}$.[62] Presumably, subsequent intramolecular or intermolecular coupling of the polarized Fe-bound NO^- induced release of $N_2O_{(g)}$, whereas acid–base reaction between the generated oxide and additional $GO_{carboxylic\ acid}$/GO_{phenol} further led to the ultimate formation of $[Fe^{3+}(L)_2(\eta^1\text{-O-GO}_{carboxylate})_4]^{n-}$ (L = $GO_{epoxide}$, $GO_{phenoxide}$, or H_2O/OH^-) in Fe:GO. Due to the weakened basicity and chelating nature of TMEDA ligand (pK_b = 5.85) in **DNIC-TMEDA**, monoprotonation of Fe-bound TMEDA by GO-derived carboxylic acid may occur followed by coordination of $GO_{carboxylate}$ to the Fe center. Subsequent deprotonation of the pendent ammonium group on Fe-bound $[H\text{-TMEDA}]^+$ and additional $GO_{carboxylic\ acid}$ by the polarized Fe-bound NO^- rationalized assembly of the $[Fe^{3+}(TMEDA)(\eta^1\text{-O-GO}_{carboxylate})_4]^{n-}$ center in Fe(TMEDA):GO accompanied by evolution of $N_2O_{(g)}$ derived from coupling of HNO. Consequently, the basicity and labile nature of $[BH_4]^-$ and NO^- ligands highlighted DNICs as a molecular precursor for deposition of the well-dispersed single-atom Fe site on GO, whereas the utilization of the chelating TMEDA ligand in **DNIC-TMEDA** played a critical role in modulating the coordination environment in the single-atom Fe site of Fe(TMEDA):GO.

Reduction of GO into rGO leading to conversion of FeSA:GO into FeSA:rGO

After the solvothermal reduction of Fe:GO/Fe(TMEDA):GO in DMF at 155 °C for 2 h, shift of PXRD diffractions peaks from 2θ = 9.0°–9.3° to 2θ = 22.9°–24.1° (SI Fig. 11) supported successful conversion of GO into rGO and preparation of Fe:rGO/Fe(TMEDA):rGO. As shown in Fig. 2a and b and SI Fig. 12, the two-dimensional sheet-like morphology as well as the flat and unspotted surface of both Fe:rGO and Fe(TMEDA):rGO were displayed in their TEM and HRTEM images. Moreover, apparent bright dots in the HAADF-STEM images combined with the intensity profile analysis of Fe:rGO and Fe(TMEDA):rGO (SI Fig. 13) indicated the retained single-atom nature of Fe sites and excluded the aggregation of Fe nanoparticles during the solvothermal treatment to Fe:GO and Fe(TMEDA):GO. Based on ICP-OES analysis, the Fe contents in Fe:rGO (Fe content = 2.4 ± 0.4 wt%) and Fe(TMEDA):rGO (Fe content = 1.5 ± 0.2 wt%) were determined to be comparable to those for Fe:GO (Fe content = 2.5 ± 0.7 wt%) and Fe(TMEDA):GO (Fe content = 1.6 ± 0.1 wt%) precursors, respectively. On the other hand, detailed discussions on the XPS/IR study of rGO, Fe:rGO, and Fe(TMEDA):rGO were included in Methods.

The electronic structure and local coordination environment of the single-atom Fe site in both Fe:rGO and Fe(TMEDA):rGO were elucidated using Mössbauer and XANES in combination with EXAFS analyses. Similar to Fe:GO and Fe(TMEDA):GO, a two-site fitting was required to simulate major doublet features observed in the Mössbauer spectra of Fe:rGO and Fe(TMEDA):rGO (Fig. 2c and d). Accordingly, the obtained Mössbauer parameters, (a) δ = 0.50 mm s^{-1} and ΔE_Q = 1.30 mm s^{-1} for site #1 (37.2%) in Fe:rGO, (b) δ = 0.49 mm s^{-1} and ΔE_Q =

Open Access Article. Published on 03 November 2025. Downloaded on 4/1/2026 3:19:42 PM.
This article is licensed under a Creative Commons Attribution-NonCommercial 3.0 Unported Licence.

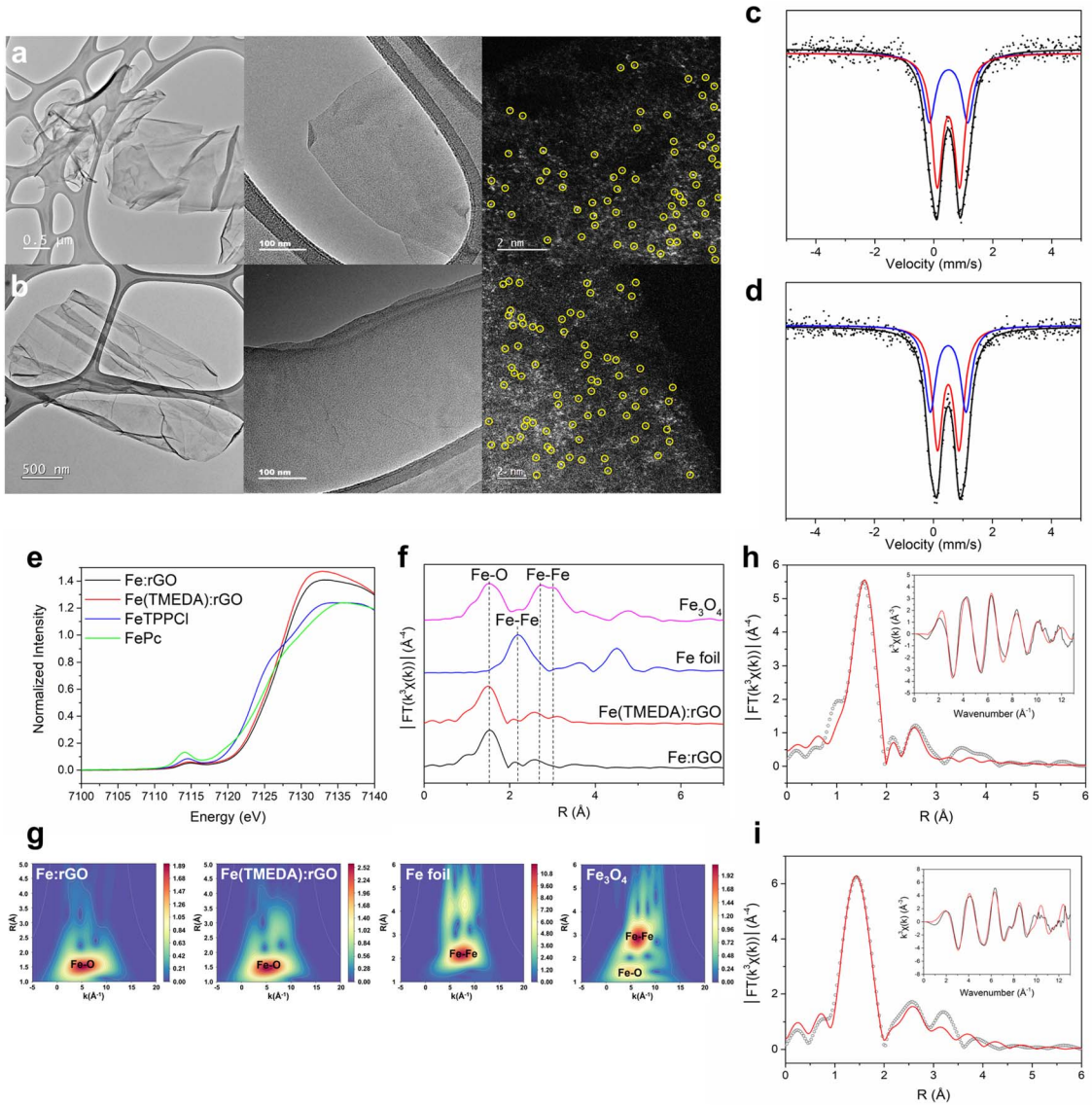

Fig. 2 Characterization of single-atom Fe on rGO (FeSA:rGO). (a and b) TEM, HRTEM, and HAADF-STEM images of (a) Fe:rGO and (b) Fe(TMEDA):rGO. The Fe single atoms are highlighted with yellow circles. (c and d) Mössbauer spectra of (c) Fe:rGO and (d) Fe(TMEDA):rGO collected at 80 K (square dots), whereas the different Fe sites are fitted in red and blue. (e) Normalized Fe K-edge XANES spectra of FePc, Fe(TPP)Cl, Fe:rGO, and Fe(TMEDA):rGO. (f) Fourier-transformed magnitudes of the experimental Fe K-edge EXAFS signals of Fe:rGO, Fe(TMEDA):rGO, Fe foil, and Fe_3O_4. (g) Wavelet transforms of k^3-weighted Fe K-edge EXAFS for Fe:rGO, Fe(TMEDA):rGO, Fe foil, and Fe_3O_4. (h and i) Phase-shift-corrected Fourier transforms (and EXAFS data, inset) and the best fits (red) of (h) Fe:rGO and (i) Fe(TMEDA):rGO.

0.76 mm s^{-1} for site #2 (62.8%) in Fe:rGO, (c) $\delta = 0.50$ mm s^{-1} and $\Delta E_Q = 0.73$ mm s^{-1} for site #1 (56.9%) in Fe(TMEDA):rGO, and (d) $\delta = 0.50$ mm s^{-1} and $\Delta E_Q = 1.21$ mm s^{-1} for site #2 (43.1%) in Fe(TMEDA):rGO, supported the high-spin Fe^{3+} center with O-/N-based ligands.[61] Moreover, the Fe^{3+} electronic structure was also evidenced by $Fe_{1s} \rightarrow Fe_{3d}$ pre-edge absorption peaks at 7114.8 eV observed in the Fe K-edge XANES spectra of both Fe:rGO and Fe(TMEDA):rGO (Fig. 2e).

Fourier-transformed magnitudes, wavelet transform (WT) plots, and EXAFS data with the best fits for Fe:rGO and Fe(TMEDA):rGO were collected in Fig. 2f, g and Table 1, whereas the detailed fitting process was listed in SI Tables 4 and 5. According to the best fits, Fe:rGO and Fe(TMEDA):rGO displayed the first-coordination shell of the Fe–O scattering path at 2.01 Å (coordination number = 6) and 1.98 Å (coordination number = 4), respectively. Moreover, chelation of TMEDA (Fe–N = 2.20 Å) was included to complete the first-coordination shell of Fe(TMEDA):rGO. In contrast to Fe foil and Fe_3O_4, the absence of formation of both (a) Fe–Fe scattering within the 2.2 Å-3.1 Å region in Fourier-transformed magnitudes and (b) Fe–Fe intensity maximum at ~6.4 $Å^{-1}$ and ~7.5 $Å^{-1}$ in WT plots for both Fe:rGO and Fe(TMEDA):rGO excluded aggregation of Fe particles and supported the single-atom nature of each Fe site. Following a similar fitting process used to simulate the first- and second-coordination shells of Fe:GO and Fe(TMEDA):GO described above, local coordination environments of the single-atom Fe sites in Fe:rGO and Fe(TMEDA):rGO were best described as $[Fe^{3+}(L)_2(\eta^1\text{-O-rGO}_{carboxylate})_4]^{n-}$ and

© 2026 The Author(s). Published by the Royal Society of Chemistry

Open Access Article. Published on 03 November 2025. Downloaded on 4/1/2026 3:19:42 PM. This article is licensed under a Creative Commons Attribution-NonCommercial 3.0 Unported Licence.

$[Fe^{3+}(TMEDA)(L)(\eta^1\text{-O-rGO}_{carboxylate})_3]^{n-}$ (L = H_2O or OH^-). That is, the local coordination environment of the well-dispersed single-atom Fe^{3+} site was retained during solvothermal treatment to Fe:GO/Fe(TMEDA):GO. As opposed to the sequential impregnation of **DNIC-BH$_4$/DNIC-TMEDA** on GO and the solvothermal reduction of Fe:GO/Fe(TMEDA):GO yielding well-dispersed single-atom Fe sites on rGO, the replacement of **DNIC-BH$_4$/DNIC-TMEDA** with $Fe(NO_3)_3$ followed by a similar solvothermal process resulted in the formation of aggregated Fe nanoparticles decorating the rGO surface (SI Fig. 16). Consequently, these findings demonstrated that DNICs, equipped with the basic and labile $[BH_4]^-$/NO^- and the chelating TMEDA ligands, can serve as efficient molecular precursors for the preparation and engineering of well-dispersed single-atom Fe^{3+}/Fe^{3+}(TMEDA) sites on (r)GO.

Magneto-electric and magneto-voltaic activity of FeSA:rGO under AMF

In magneto-catalysis, an electrically conductive substrate (*i.e.* rGO) can serve as a magneto-sensitizer (a) to harness the energy from an alternating magnetic field (AMF), (b) to induce the electric current based on the Lenz's law, and (c) to potentially generate the unexplored magneto-voltaic activity. Moreover, an electronically coupled active site (*i.e.* single-atom Fe) on the substrate can be designed to promote selective chemical reactions. In the attempt to evaluate the potential of FeSA:(r)GO as a magneto-catalyst, (a) the energy band diagram, (b) electric conductivity, (c) AMF-induced electric current, and (d) magneto-voltaic properties of these materials were established/measured.

As shown in the solid-state UV-vis spectrum for Fe:rGO (or Fe(TMEDA):rGO, SI Fig. 17a), the absorption peak at 256 nm (or 258 nm) was ascribed to the π-to-π* transition derived from the sp^2-hybridized C=C moiety in the rGO substrate. Solid-state UV-vis spectra for Fe:rGO and Fe(TMEDA):rGO were further processed into Tauc plots in order to determine the band gap (E_g) for these Fe-based SACs (SI Fig. 17b and c). Based on the intercepts on the *X*-axis for extrapolated linear lines in Tauc plots, Fe:rGO and Fe(TMEDA):rGO featured band gaps (E_g) of 3.06 eV and 3.00 eV, respectively, which were comparable to the reported E_g of 3.10 eV for rGO.[63] On the other hand, based on the oxidation onset potentials of 2.21 V and 2.23 V (*vs.* Ag/AgCl) displayed by Fe:rGO and Fe(TMEDA):rGO (SI Fig. 18), E_{HOMO} values for Fe:rGO and Fe(TMEDA):rGO were calculated to be 2.41 eV and 2.43 eV (*vs.* SHE), respectively.[64] Consequently, the energy band structure for (a) Fe:rGO was characterized as E_{HOMO} = 2.41 eV, E_g = 3.06 eV, and E_{LUMO} = −0.65 eV, and (b) Fe(TMEDA):rGO was identified as E_{HOMO} = 2.43 eV, E_g = 3.00 eV, and E_{LUMO} = −0.57 eV (Scheme 2). That is, the nature of the rGO supporting material dictated the energy band structure for FeSA:rGO.

According to the measured electric conductivity, solvothermal reduction of GO/Fe:GO/Fe(TMEDA):GO into rGO/Fe:rGO/Fe(TMEDA):rGO successfully enhanced electric conductivity from 2.40×10^{-6}/3.26×10^{-6}/8.50×10^{-6} S cm^{-1} to 0.34 ± 0.01/0.45 ± 0.19/0.54 ± 0.17 S cm^{-1}. Upon application of AMF to electrically conductive rGO and FeSA:rGO, in comparison with GO and FeSA:GO, AMF-induced generation of electric current reflected on a luminous light-emitting diode (LED, SI Fig. 19a). Moreover, intermittent generation of an eddy current of 148.3 ± 6.3 μA synchronized with the ON/OFF-switch on application of AMF (1.1 cm coil, 0.64 kW, 1.58 mT) to rGO demonstrated an instantaneous magnetic-responsive nature of the rGO substrate (Fig. 3d and Table 2). Of importance, Fe:rGO

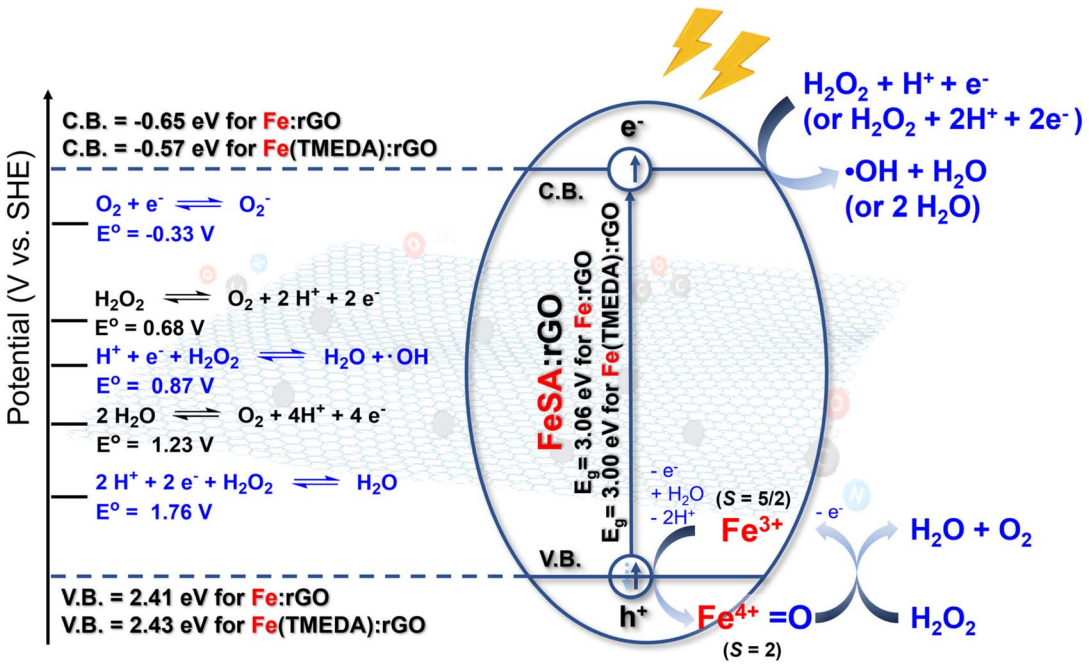

Scheme 2 Energy band diagram for FeSA:rGO and proposed mechanisms for magneto-catalytic transformation of H_2O_2 into O_2 mediated by FeSA:rGO under an AMF.[65]

Open Access Article. Published on 03 November 2025. Downloaded on 4/1/2026 3:19:42 PM. This article is licensed under a Creative Commons Attribution-NonCommercial 3.0 Unported Licence.

and Fe(TMEDA):rGO displayed similar AMF-induced generation of electric current of 151.8 ± 5.0 μA and 147.2 ± 3.9 μA (Fig. 3e and f), respectively, which was in contrast to the 1.6 ± 0.9 μA/0.4 ± 0.1 μA/0.3 ± 0.1 μA exhibited by GO/Fe:GO/Fe(TMEDA):GO (Fig. 3a–c). When the AMF power was raised from 0.64 kW to 1.60 kW (or 2.24 kW), the increase of electric current generated in rGO/Fe:rGO/Fe(TMEDA):rGO demonstrated AMF power as a remote control to tailor the intensity of generated electric current (Fig. 3d–f and Table 2). In contrast, negligible response of generated electric current to the change of AMF power was observed in the less electrically conductive GO, Fe:GO, and Fe(TMEDA):GO (Fig. 3a–c).

As shown in SI Fig. 20a, sine waves with a wide range of frequency for AMF-induced generation of output voltage were observed during application of AMF to rGO and FeSA:rGO, which was due to the high-frequency nature of AMF. In the absence of magneto-sensitizer materials (*i.e.* rGO or FeSA:rGO), no AMF-induced electric voltage was observed, which confirmed that the perturbation of AMF on the oscilloscope was minimal (SI Fig. 19d). In order to extract the real AMF-induced generation of electric voltage in rGO and FeSA:rGO, a Fast Fourier transform process to the original *V*–*t* curves was performed to obtain the frequency spectra (SI Fig. 20b). Moreover, the peaks with a frequency of ~0.94 MHz, which lay in the range of 0.75–1.15 MHz for AMF, were selected to obtain processed *V*–*t* curves through a further reverse Fast Fourier transform process (Fig. 3g–i). According to the data processing procedure described above, generation of electric voltage upon application of different AMF power to rGO, Fe:rGO, and Fe(TMEDA):rGO was collected in Table 2. Similar to the dependence of AMF-induced electric current on AMF power, increase of AMF-induced electric voltage was observed upon elevation of AMF power applied to rGO and FeSA:rGO. Based on the investigations discussed above, the nature and electric conductivity of the rGO/GO substrate can serve as an ON/OFF switch on controlling AMF-induced generation of electric current and voltage, whereas the intensity of generated electric current and voltage remained tailored by the AMF power.

Mechanistic and kinetic investigations on magneto-catalytic conversion of H_2O_2 into O_2 promoted by FeSA:rGO under AMF

Inspired by the magneto-electric and magneto-voltaic effects of electrically conductive rGO and FeSA:rGO triggered by AMF, magneto-catalytic activity of these materials was explored using H_2O_2 as a potentially dual reductant and oxidant (Scheme 2). In addition, considering the elevated production of H_2O_2 (~100 μM) under hypoxic and acidic tumor microenvironments (≤2% O_2, pH 6.0–6.5),[45–51,66] magneto-catalytic conversion of H_2O_2 and

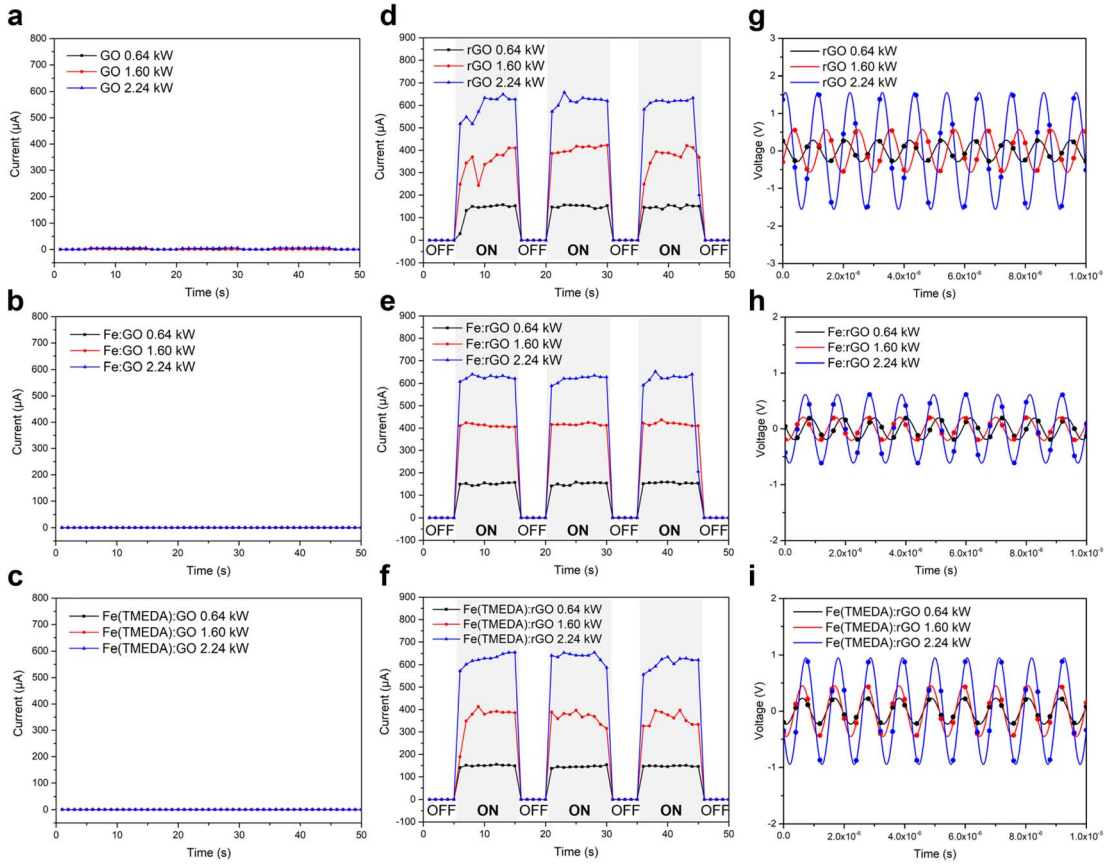

Fig. 3 Magneto-electric and magneto-voltaic activity of GO, FeSA:GO, rGO, and FeSA:rGO under AMF. (a–f) *I*–*t* curves for (a) GO, (b) Fe:GO, (c) Fe(TMEDA):GO, (d) rGO, (e) Fe:rGO, and (f) Fe(TMEDA):rGO under intermittent application of AMF at 0.64 kW (black), 1.60 kW (red), and 2.24 kW (blue). (g–i) Processed (dots) and simulated *V*–*t* curves (lines) for (g) rGO, (h) Fe:rGO, and (i) Fe(TMEDA):rGO under application of AMF at 0.64 kW (black), 1.60 kW (red), and 2.24 kW (blue).

© 2026 The Author(s). Published by the Royal Society of Chemistry

Open Access Article. Published on 03 November 2025. Downloaded on 4/1/2026 3:19:42 PM. This article is licensed under a Creative Commons Attribution-NonCommercial 3.0 Unported Licence.

Table 2 Magneto-driven electric current/voltage and rate for magneto-catalytic evolution of O_2 upon application of different power of AMF to rGO and FeSA:rGO

Magneto-driven electric current (μA)			
	AMF power		
Material	0.64 kW	1.60 kW	2.24 kW
rGO	148.3 ± 6.3	375.1 ± 49.9	596.5 ± 81.8
Fe:rGO	151.8 ± 5.0	416.1 ± 06.9	610.3 ± 77.5
Fe(TMEDA):rGO	147.2 ± 3.9	363.6 ± 41.5	623.5 ± 26.0

Magneto-driven electric voltage (V)			
	AMF power		
Material	0.64 kW	1.60 kW	2.24 kW
rGO	0.29	0.57	1.56
Fe:rGO	0.19	0.21	0.62
Fe(TMEDA):rGO	0.23	0.45	0.95

Rate for magneto-catalytic evolution of O_2 (μM min^{-1})			
	AMF power		
Material	0.32 kW	0.96 kW	1.60 kW
Fe:rGO	0.313 ± 0.084	0.719 ± 0.044	0.984 ± 0.109
Fe(TMEDA):rGO	0.719 ± 0.106	1.062 ± 0.141	1.844 ± 0.831

evolution of O_2 promoted by rGO/FeSA:rGO was elucidated in 50 mM potassium phosphate buffer (pH 6.5). Kinetic profiles for time-dependent consumption of H_2O_2 (100 μM) mediated by rGO or FeSA:rGO without/with application of AMF are depicted in Fig. 4a and b. As opposed to limited consumption of H_2O_2 mediated by rGO without/with the application of AMF, both Fe:rGO and Fe(TMEDA):rGO displayed activity for decomposition of H_2O_2. Upon application of AMF, moreover, enhanced and complete decomposition of H_2O_2 induced by Fe:rGO (or Fe(TMEDA):rGO) was observed after reaction for 3 h. Consequently, these H_2O_2-consumption investigations unraveled the critical role of single-atom Fe active sites in FeSA:rGO, whereas the magneto-voltaic activity triggered by AMF further boosted the catalytic activity.

Mechanisms for reported transformations of H_2O_2 without additional biological substrates were collected in Scheme 2, which included (a) two-electron oxidation of H_2O_2 into O_2 promoted by catalase or artificial nanomaterials,[52,53,57] (b) two-electron reduction of H_2O_2 into H_2O catalysed by catalase, and (c) one-electron reduction of H_2O_2 into H_2O and $^{\bullet}OH$ *via* Fenton reaction.[54–57,67] Regarding the low concentration of O_2 (≤2% O_2) and high concentration of H_2O_2 (~100 μM) under a tumor microenvironment,[45–51,66] consequently, FeSA:rGO-induced two-electron oxidation of H_2O_2 leading to evolution of O_2 was explored.

As shown in Fig. 4c and d, no formation of O_2 was observed in the reaction of H_2O_2 and FeSA:rGO, despite the decomposition of H_2O_2 under the conditions described above. In contrast, external application of AMF to H_2O_2 (100 μM) in the presence of Fe:rGO (or Fe(TMEDA):rGO) initiated a steady formation of O_2 reaching a plateau at 1.84 ± 0.66 ppm (or 2.13 ± 0.71 ppm). Inspired by the distinctive oxygen evolution reaction (OER) upon application of AMF to H_2O_2 and Fe:rGO (or Fe(TMEDA):rGO), concentration of H_2O_2 was increased from 100 μM to 500 μM in an attempt to quantify the proportion of H_2O_2 transformed into O_2, which was complicated by the deviation of low O_2 concentration described above. Upon the application of AMF to a 500 μM H_2O_2 aqueous solution in the presence of Fe:rGO (or Fe(TMEDA):rGO), the decomposition of 493.4 ± 2.6 μM (or 483.9 ± 5.1 μM) of H_2O_2 was observed, accompanied by the evolution of 5.36 ± 0.20 ppm (or 5.80 ± 0.24 ppm) of O_2. This AMF-induced evolution of O_2 was further confirmed by GC analysis (SI Fig. 21). Based on the evolution of 5.36 ± 0.20 ppm/155.4 ± 5.8 μM (or 5.80 ± 0.24 ppm/168.2 ± 6.96 μM) of O_2, that is, around one-third of H_2O_2 was oxidized into O_2 upon application of AMF to H_2O_2 in the presence of Fe:rGO (or Fe(TMEDA):rGO). On the other hand, O_2 evolution profiles for magneto-catalytic OER derived from the reaction of Fe(TMEDA):rGO and H_2O_2 under pH 5.5, 6.5, and 7.4 with or without the presence of 1 mM GSH or 10 mM lactate are depicted in SI Fig. 22. Comparable magneto-catalytic OER observed under these simulated conditions demonstrated the potential applicability of FeSA:rGO toward magneto-catalytic conversion of H_2O_2 into O_2 under the tumor microenvironment.[68,69]

Besides the magneto-catalytic efficiency for the OER, the recyclability of Fe:rGO and Fe(TMEDA):rGO as magneto-catalysts was evaluated through a repeated use study. During the recyclability study, Fe:rGO (or Fe(TMEDA):rGO) exhibited a gradual decrease in magneto-catalytic OER activity, retaining approximately 87% (or 85%) of its initial activity over seven (or five) consecutive cycles (Fig. 4e and f and SI Table 6). After the magneto-catalytic OER cycles, the Fe content in the recovered Fe:rGO was determined to be 2.0 ± 0.1 wt%, which corresponded to ~83% of that in the as-prepared Fe:rGO (2.4 ± 0.4 wt%). In addition, the used Fe:rGO (or Fe(TMEDA):rGO) retained consistent HRTEM/HAADF-STEM images and XANES/EXAFS spectra when compared with those of the as-prepared FeSA:rGO (SI Fig. 23 and 24). On the other hand, the supernatant solution collected after each cycle displayed no detectable magneto-catalytic OER activity (SI Fig. 25). These results suggested that the slight but unavoidable leaching of Fe ions accounted for the gradual decline in magneto-catalytic OER activity observed over successive cycles, while the well-dispersed single-atom Fe^{3+} centers preserved in FeSA:rGO remained catalytically active in promoting the magneto-catalytic OER.

Inspired by the magneto-catalytic OER initiated by the application of AMF to an aqueous solution of H_2O_2 and FeSA:rGO, the dependence of FeSA:rGO-promoted magneto-catalytic OER rates on (a) FeSA:rGO concentration, (b) H_2O_2 concentration, (c) AMF power intensity, and (d) FeSA:rGO physical form (*i.e.* dispersed powders *vs.* bulk pellet) was systematically investigated. The natural logarithmic plots of OER rates *versus* the concentration of Fe:rGO (or Fe(TMEDA):rGO) are shown in Fig. 4g and h. The obtained slopes of 1.049 for Fe:rGO and 0.927 for Fe(TMEDA):rGO supported that

Open Access Article. Published on 03 November 2025. Downloaded on 4/1/2026 3:19:42 PM.
This article is licensed under a Creative Commons Attribution-NonCommercial 3.0 Unported Licence.

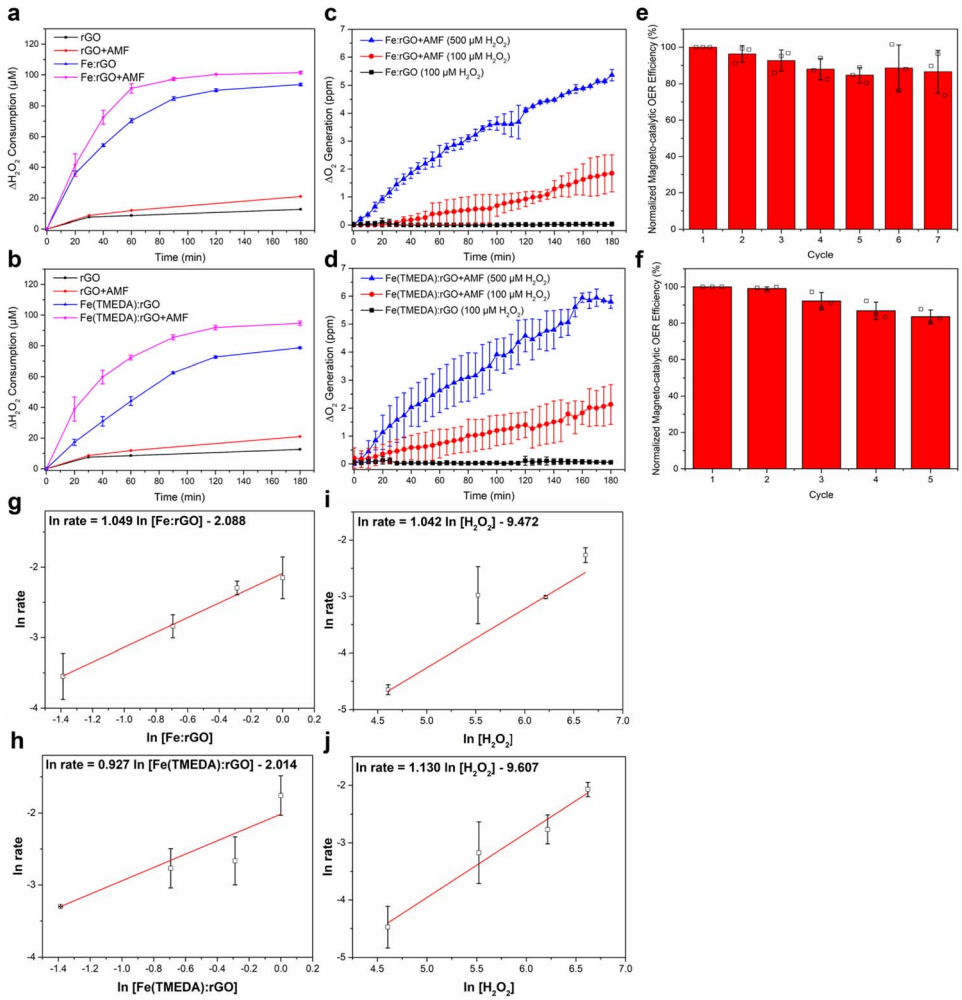

Fig. 4 Recyclability and kinetic study on magneto-catalytic conversion of H_2O_2 into O_2 promoted by FeSA:rGO. (a and b) Time-dependent consumption of H_2O_2 mediated by (a) Fe:rGO and (b) Fe(TMEDA):rGO in 50 mM potassium phosphate buffer (pH 6.5) without (blue) and with (magenta) application of AMF. Time-dependent consumption of H_2O_2 mediated by rGO without and with application of AMF was depicted in black and red. (c and d) Time-dependent evolution of O_2 upon treatment of H_2O_2 (100 μM in black/red or 500 μM in blue) to (c) Fe:rGO and (d) Fe(TMEDA):rGO in 50 mM potassium phosphate buffer (pH 6.5) without (black) and with (red or blue) application of AMF. (e and f) Normalized magneto-catalytic OER efficiency during the multiple-cycle reusability test of (e) Fe:rGO and (f) Fe(TMEDA):rGO. Magneto-catalytic OER activity of Fe:rGO and Fe(TMEDA):rGO was normalized to that of the as-prepared Fe:rGO and Fe(TMEDA):rGO, respectively. (g and h) Natural logarithmic plot of O_2 evolution rate *versus* concentration of (g) Fe:rGO and (h) Fe(TMEDA):rGO under application of AMF (1.6 kW) to the aqueous solution of H_2O_2 (750 μM). (i and j) Natural logarithmic plot of O_2 evolution rate *versus* concentration of H_2O_2 under application of AMF (1.6 kW) to the aqueous solution of (i) Fe:rGO (1 mg mL^{-1}) and (j) Fe(TMEDA):rGO (1 mg mL^{-1}). Data show the mean ± standard deviation (SD) from three independent experiments.

the magneto-catalytic OER followed a first-order kinetics relative to the concentration of FeSA:rGO. The dependence of the magneto-catalytic OER rates on the concentration of H_2O_2 was studied in a similar manner. As illustrated in Fig. 4i–j, a first-order dependence on H_2O_2 concentration was evidenced by the observed slopes of 1.042 for Fe:rGO and 1.130 for Fe(TMEDA):rGO in the plots of ln(rate) *versus* ln([H_2O_2]). Accordingly, the rate law for the magneto-catalytic OER was best described as rate ∝ $[FeSA:rGO]^1[H_2O_2]^1$, which indicated the participation of both FeSA:rGO and H_2O_2 in the rate-determining step of the magneto-catalytic OER. As collected in Table 2, raising the applied AMF power from 0.32 kW to 0.96 kW and 1.6 kW resulted in a significant enhancement of the magneto-catalytic OER rates. Specifically, the magneto-catalytic OER rates increased from 0.313 ± 0.084 μM min^{-1} to 0.719 ± 0.044 μM min^{-1} and 0.984 ± 0.109 μM min^{-1} for Fe:rGO, and from 0.719 ± 0.106 μM min^{-1} to 1.062 ± 0.141 μM min^{-1} and 1.844 ± 0.831 μM min^{-1} for Fe(TMEDA):rGO. These findings suggested that AMF power acted as both kinetic and thermodynamic driving forces enhancing the AMF-induced electric current and magneto-voltaic activity of FeSA:rGO, which, in turn, effectively transferred these elevated driving forces to accelerate the magneto-catalytic evolution of O_2 from H_2O_2. The potential effect of magneto-catalyst physical form (*i.e.* dispersed powders *vs.* bulk pellet) on the magneto-catalytic OER rates was also elucidated. Upon application of AMF (1.6 kW) to an aqueous

© 2026 The Author(s). Published by the Royal Society of Chemistry

Open Access Article. Published on 03 November 2025. Downloaded on 4/1/2026 3:19:42 PM. This article is licensed under a Creative Commons Attribution-NonCommercial 3.0 Unported Licence.

solution of H_2O_2 (750 μM) containing Fe(TMEDA):rGO, the rates for magneto-catalytic O_2 evolution decreased from 3.963 ± 0.481 μM min^{-1} (dispersed powders) to 2.950 ± 0.644 μM min^{-1} when using Fe(TMEDA):rGO in a bulk pellet form (SI Fig. 26). This reduced magneto-catalytic activity, presumably, could be attributed to the lower accessible surface area of Fe(TMEDA):rGO in the bulk pellet compared to the well-dispersed powder. Based on the investigations discussed above, (a) the concentration of FeSA:rGO, (b) the concentration of H_2O_2, (c) the power intensity of AMF and (d) the physical form of FeSA:rGO played a key role in controlling the rates for FeSA:rGO-promoted magneto-catalytic OER.

After optimizing the magneto-catalytic OER efficiency of FeSA:rGO as described above, Fe(TMEDA):rGO (or Fe:rGO) displayed a rate of 3.96 μM min^{-1} (or 3.25 μM min^{-1}) for magneto-catalytic OER (SI Table 6), which corresponded to a turnover frequency (TOF) of 0.015 min^{-1} (or 0.008 min^{-1}) based on the Fe content in Fe(TMEDA):rGO (or Fe:rGO). Presumably, the superior magneto-catalytic activity of Fe(TMEDA):rGO, in comparison with Fe:rGO, could be rationalized by the distinct coordination environments of the single-atom Fe sites, namely $[Fe^{3+}(TMEDA)_2(\eta^1\text{-O-GO}_{carboxylate})_4]^{n-}$ in Fe(TMEDA):rGO *versus* $[Fe^{3+}(H_2O)_2(\eta^1\text{-O-GO}_{carboxylate})_4]^{n-}$ in Fe:rGO. Relevant to molecular complexes with high-valent Fe^{IV}=O electronic structure,[70–72] the stronger electron-donating ability of the bidentate TMEDA ligand in Fe(TMEDA):rGO may facilitate oxidation of the Fe^{3+} center and stabilization of the transient Fe^{4+} intermediate during magneto-catalysis, of which the mechanism is discussed below. On the other hand, a variety of MnO_2-based nanozymes and Fe-based SACs have been reported for the catalytic conversion of H_2O_2 into O_2.[52,53,73–78] As summarized in SI Table 6, MnO_2-based nanozymes featured a wide range of OER rates (1.33–320.6 μM min^{-1}), which may primarily be attributed to the kinetic dependence of OER rates on the concentrations of MnO_2-based nanozymes and H_2O_2 substrates (0.1–125 mM). Meanwhile, reported Fe-based SACs exhibited comparable OER rates (10.4–166.2 μM min^{-1}) yet exceptionally high TOFs (60.6–1031.1 min^{-1}) under 1–100 mM H_2O_2, thereby reflecting the superior atomic utilization efficiency derived from atomically dispersed Fe–N_4 active sites. These results underscored the robust nature of MnO_2-based nanozymes and Fe-based SACs for rapid OER under high H_2O_2 concentrations. When benchmarked against these state-of-the-art systems, FeSA:rGO demonstrated (a) comparable catalytic stability under simulated biological conditions (500 μM H_2O_2 at pH 6.5) and (b) a unique ability for remote and ON/OFF-switchable control of the OER through the application of AMF.

In the reported studies, a variety of Fe–N_4 single-atom nanozymes has been explored for catalase-like activity.[77,80,81] Despite differences in the structural design of Fe–N_4 active centers anchored on various supporting materials, DFT calculations from these studies have consistently demonstrated that these Fe–N_4 single-atom nanozymes shared a common electron-deficient and high-valent Fe^{4+} intermediate, which was the crucial active intermediate responsible for the catalytic conversion of H_2O_2 into O_2. Specifically, the binding of H_2O_2 to the Fe^{4+} center followed by deprotonation of the Fe-bound H_2O_2 resulted in the formation of an $[Fe^{4+}\text{-}O_2^{2-}]$ intermediate. Subsequent intramolecular electron transfer from the O_2^{2-} moiety to the Fe^{4+} center induced evolution of O_2 and regeneration of the Fe^{2+} species, which was further oxidized to the Fe^{4+} state for reaction with another equivalent of H_2O_2. In comparison with the Fe–N_4 single-atom nanozymes discussed above, the $[Fe^{3+}(L)(\eta^1\text{-O-GO}_{carboxylate})_4]^{n-}$ (L = TMEDA or $(OH_2)_2$) resting state in the as-prepared FeSA:rGO was found to be catalytically inert toward the O_2 evolution reaction in the absence of AMF. Upon AMF application promoting a charge separation process in FeSA:rGO, in contrast, the low-lying electron holes generated in AMF-activated FeSA:rGO (at 2.41 eV *vs.* SHE for Fe:rGO and at 2.43 eV *vs.* SHE for Fe(TMEDA):rGO) may serve as an additional driving force to facilitate oxidation of the Fe^{3+} resting state and transient formation of a single-atom Fe^{4+} center, a potentially active species responsible for conversion of H_2O_2 into O_2.

In an attempt to probe transient formation of the proposed Fe^{4+} intermediate during magneto-catalysis, an aqueous solution containing Fe:rGO (or Fe(TMEDA):rGO) and H_2O_2 was subjected to AMF (1.6 kW) for 1 min (or 0.5 min) and immediately freeze-quenched (FQ) in $N_{2(l)}$. The FQ-trapped intermediate(s) was further analyzed using Fe K-edge XANES. As shown in Fig. 5a and b, an $Fe_{1s} \rightarrow Fe_{3d}$ pre-edge absorption peak at 7114.8 eV was observed in the XANES spectrum of Fe:rGO (or Fe(TMEDA):rGO) in the resting state, which was characteristic of an Fe^{3+} electronic structure. During the magneto-catalytic reaction under AMF, a notable shift of the pre-edge absorption peak to 7115.1 eV suggested oxidation of the Fe^{3+} center to a higher oxidation state. Through further deconvolution of the pre-edge features in these Fe K-edge XANES spectra (Fig. 5c–f), a distinctive Fe_{1s}-to-Fe_{3d} absorption peak at 7116.3 eV (or 7116.1 eV) was revealed in the Fe:rGO (or Fe(TMEDA):rGO) under magneto-catalysis, which supported the formation of an Fe^{4+} intermediate.[82,83] As discussed above, the original Fe_{1s}-to-Fe_{3d} pre-edge absorption peak at 7114.8 eV was recovered after the magneto-catalytic process (SI Fig. 24).

Under a similar methodology, X-band EPR and Mössbauer spectroscopic investigations on the as-prepared FeSA:rGO and the FQ-trapped intermediate(s) were performed to provide additional support for the transient formation of Fe^{4+} species during magneto-catalysis. As shown in Fig. 5g–h, both as-prepared Fe:rGO and Fe(TMEDA):rGO exhibited signals at $g \approx 4.3$ in the perpendicular-mode EPR spectra at 4.7 K, which were consistent with the high-spin Fe^{3+} electronic structure in the resting state. Upon application of AMF for 5 min (or 10 min), a significant decrease of these perpendicular-mode EPR signals occurred accompanied by time-dependent formation of a broad valley at $g \approx 4.1$ in the EPR spectra measured in the parallel mode. These parallel-mode EPR signals at $g \approx 4.1$ corresponded to the $|\pm1\rangle$ doublet of a high-spin Fe^{4+} ($S = 2$) species.[84] In addition, the absence of a signal at $g \approx 8$, associated with the $|\pm2\rangle$ doublet, may be ascribed to a nearly axial zero-field splitting (E/D < 0.01),[85,86] suggesting a low-rhombicity ligand field around the single-atom Fe^{4+} center. The Mössbauer spectrum of the FQ intermediate(s), obtained after application of AMF (1.6 kW) to the Fe:rGO/H_2O_2 system for 10 min, is shown in SI Fig.

Open Access Article. Published on 03 November 2025. Downloaded on 4/1/2026 3:19:42 PM.
This article is licensed under a Creative Commons Attribution-NonCommercial 3.0 Unported Licence.

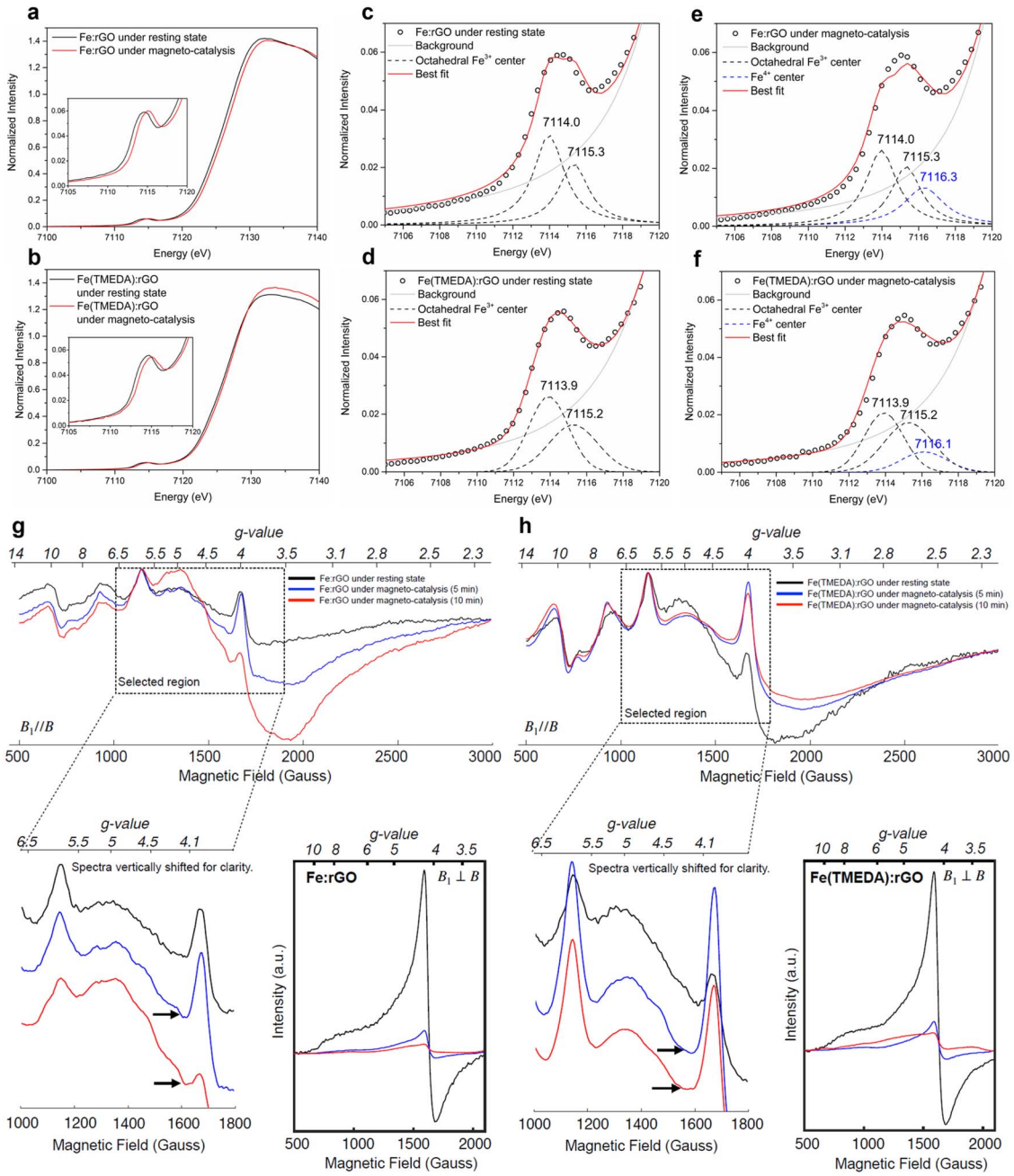

Fig. 5 *Ex situ* XANES and EPR identification of a high-valent Fe^{4+} intermediate during magneto-catalytic conversion of H_2O_2 into O_2 promoted by FeSA:rGO under AMF. (a and b). Normalized Fe K-edge XANES spectra for (a) Fe:rGO and (b) Fe(TMEDA):rGO in the resting state (black) and under magneto-catalysis (red). Enlarged Fe_{1s}-to-Fe_{3d} pre-edge regions are shown in the inset. (c–f) Deconvolutions of Fe_{1s}-to-Fe_{3d} pre-edge features for (c) Fe:rGO in the resting state, (d) Fe(TMEDA):rGO in the resting state, (e) Fe:rGO under magneto-catalysis, and (f) Fe(TMEDA):rGO under magneto-catalysis. Experimental data (empty circle), the background function (gray line), the pre-edge peaks from the fit to an octahedral Fe^{3+} center (black dashed line), the pre-edge peaks from the fit to an Fe^{4+} center (blue dashed line), and the fit to the data (red line). Following the reported deconvolution of Fe_{1s}-to-Fe_{3d} pre-edge features for high-spin Fe^{3+} complexes with an octahedral geometry,[79] the Fe_{1s}-to-Fe_{3d} pre-edge features of Fe:rGO (or Fe(TMEDA):rGO) in the resting state were fitted with two peaks derived from Fe_{1s}-to-$Fe_{3d(t2g)}$ and Fe_{1s}-to-$Fe_{3d(eg)}$ transitions. Through comparison with Fe:rGO (or Fe(TMEDA):rGO) in the resting state, the additional peak feature observed in Fe:rGO (or Fe(TMEDA):rGO) under magneto-catalysis was fitted with one peak due to the lack of detailed information for the coordination environment of the Fe^{4+} intermediate. (g and h) X-band EPR spectra of (g) Fe:rGO and (h) Fe(TMEDA):rGO after exposure to AMF for 5 min (blue)/10 min (red) and freeze-quenched in $N_{2(l)}$. These spectra were recorded in both parallel mode (B_1//B, upper panels) and perpendicular mode ($B_1 \perp B$, lower right panels). The X-band EPR spectra of the as-prepared Fe:rGO and Fe(TMEDA):rGO were depicted in black. In the perpendicular-mode spectra, the characteristic high-spin Fe^{3+} signals at $g \approx 4.3$ were significantly reduced after exposure to AMF. In the parallel-mode EPR spectra, in comparison with the as-prepared Fe:rGO and Fe(TMEDA):rGO, a broad valley feature centered around $g \approx 4.1$ appeared after exposure to AMF. Expanded views of the parallel-mode EPR spectra in the region between $g \approx 3.5$ and $g = 6.7$ were displayed in the lower left panels, with the spectra vertically displaced for clarity. Arrows indicated spectral differences near $g \approx 4.1$. To facilitate direct comparison of spectral profiles, the parallel-mode spectra in the upper panels were normalized to their maximum intensity, while the corresponding raw and unnormalized spectra were provided in SI Fig. 28. All spectra were recorded at 4.7 K.

© 2026 The Author(s). Published by the Royal Society of Chemistry

Open Access Article. Published on 03 November 2025. Downloaded on 4/1/2026 3:19:42 PM. This article is licensed under a Creative Commons Attribution-NonCommercial 3.0 Unported Licence.

27. Based on the two-site fitting, the Fe^{3+} center displayed a doublet signal with an isomer shift (δ) of 0.47 mm s^{-1} and a quadrupole splitting (ΔE_Q) of 0.84 mm s^{-1}, which was consistent with a high-spin Fe^{3+} species. In contrast, an additional doublet signal with an isomer shift (δ) of −0.04 mm s^{-1} and a quadrupole splitting (ΔE_Q) of 0.80 mm s^{-1} supported the formation of an Fe^{4+} intermediate.[87–89] Based on the FQ-XANES, FQ-Mössbauer, and FQ-EPR experiments discussed above, consequently, transient formation of a high-spin Fe^{4+} intermediate *via* AMF-induced activation of FeSA:rGO and oxidation of the Fe^{3+} resting state served as the critical step for magneto-catalytic oxidation of H_2O_2 and evolution of O_2.

Recently, during the AMF-enhanced electrocatalytic OER from H_2O *via* the adsorbate evolution mechanism, spin-selective electron removal from the σ_{M-O} and σ_{O-H} bonds in the singlet M-OOH intermediate was reported to lower the kinetic barrier for oxidation of M-bound $[OOH]^-$ into released triplet O_2.[27,37–40] In this study, the AMF-dependent spin polarization effect on magneto-catalytic OER was elucidated by comparing the raw and unnormalized parallel-mode X-band EPR spectra of Fe:rGO and Fe(TMEDA):rGO under resting and magneto-catalytic conditions, respectively. As shown in SI Fig. 28, the spectra for Fe:rGO and Fe(TMEDA):rGO under magneto-catalytic conditions exhibited a higher signal intensity (including the EPR signal at $g \approx 4.1$) than those obtained in the resting state. These enhancements in EPR signal amplitudes under AMF, presumably, were attributed to field-induced parallel spin alignment in Fe:rGO and Fe(TMEDA):rGO. Accordingly, in addition to oxidation of H_2O_2 thermodynamically driven by the magneto-voltaic activity of FeSA:rGO described above, AMF-induced spin polarization effects may serve as another mechanism for kinetically promoting FeSA:rGO-mediated OER from H_2O_2 under AMF. On the other hand, magnetic heating of rGO, Fe:rGO/Fe(TMEDA):rGO, and Pt:rGO was excluded according to the limited change of local temperature of these materials under AMF ($\Delta T = 0.7$–1.9 °C, SI Fig. 29),[26–33] which further ruled out magneto-thermally enhanced transformation of H_2O_2.

Based on the discussion above, two-electron oxidation of H_2O_2 into O_2 was discovered to serve as the oxidation half-reaction promoted by FeSA:rGO under AMF. To balance the magneto-catalytic redox transformation of H_2O_2 (Scheme 2), one-electron (or two-electron) reduction of H_2O_2 into $^{\bullet}OH$ and H_2O (or solely into H_2O) was further investigated. 5,5-Dimethyl-1-pyrroline *N*-oxide (DMPO) in combination with EPR spectroscopy and methylene blue in combination with UV-vis spectroscopy were utilized to detect potential formation of transient $^{\bullet}OH$ species derived from FeSA:rGO-induced reduction of H_2O_2.[25,90] During FeSA:rGO-induced reduction of H_2O_2 without/with application of AMF, transient formation of $^{\bullet}OH$ species was trapped by DMPO yielding DMPO-OH as evidenced by the characteristic quartet EPR signals with a 1:2:2:1 intensity (SI Fig. 30). As opposed to the inert nature of methylene blue towards H_2O_2 (SI Fig. 31), degradation of methylene blue was observed upon treatments of Fe:rGO/Fe(TMEDA):rGO (1 mg mL^{-1}) with H_2O_2 (100 μM) without/with application of AMF at 1.6 kW (SI Fig. 32), which was attributed to transient formation of $^{\bullet}OH$ species. Of interest, application of a lower AMF at 0.96 kW to Fe(TMEDA):rGO (0.25 mg mL^{-1}) and H_2O_2 (500 μM) led to limited generation of $^{\bullet}OH$ while maintaining steady evolution of O_2. Accordingly, the mechanism for magneto-catalytic decomposition of H_2O_2 was best described as two-electron oxidation of H_2O_2 into O_2 promoted by FeSA:rGO under AMF coupled with one-electron reduction of H_2O_2 into $^{\bullet}OH$ and H_2O (or two-electron reduction of H_2O_2 solely into H_2O, Scheme 2). Moreover, magneto-catalytic evolution of O_2 coupled with or without generation of $^{\bullet}OH$ remained controlled by the AMF power, H_2O_2 concentration, and FeSA:rGO concentration. Under the non-application of AMF to FeSA:rGO, on the other hand, activation of H_2O_2 by FeSA:rGO for oxygenation of the rGO substrate yielding released $CO_{2(g)}$ and oxidized rGO was evidenced by GC and XPS analyses (SI Fig. 33). That is, in the absence of AMF, the rGO substrate served as a sacrificial reductant to promote FeSA:rGO-mediated reduction of H_2O_2 into $^{\bullet}OH$ and H_2O without evolution of O_2.[91]

Conclusions

In this study, investigations on magneto-voltaic and magneto-catalytic activity of FeSA:(r)GO for conversion of H_2O_2 into O_2 have led to the following results:

1. Relying on the basicity and labile nature of $[BH_4]^-$ and NO^- ligands as well as the chelating properties of the TMEDA ligand in Fe complexes **DNIC-BH$_4$** and **DNIC-TMEDA**, reactions of these DNICs with GO were explored for one-step and pyrolysis-free preparation of Fe:GO and Fe(TMEDA):GO, respectively. Based on the spectroscopic and imaging characterization, Fe:GO was best described as a two-dimensional sheet-like GO decorated with well-dispersed single-atom Fe featuring an $[Fe^{3+}(H_2O)_2(\eta^1\text{-O-GO}_{carboxylate})_4]^{n-}$ local coordination environment. In comparison, single-atom Fe centers in Fe(TMEDA):GO displayed an $[Fe^{3+}(TMEDA)_2(\eta^1\text{-O-GO}_{carboxylate})_4]^{n-}$ local coordination geometry. That is, different supporting ligands in **DNIC-BH$_4$** and **DNIC-TMEDA** modulated the transformation mechanisms for these Fe precursors during their reactions with GO and controlled the distinctive coordination environments for single-atom Fe centers in Fe:GO and Fe(TMEDA):GO.

2. Through solvothermal reduction of Fe:GO/Fe(TMEDA):GO, Fe:rGO/Fe(TMEDA):rGO was successfully synthesized with retained geometric and electronic structure for well-dispersed single-atom Fe centers. The GO-to-rGO transformation enhanced the electric conductivity from 3.26–8.50 × 10^{-6} S cm^{-1} for Fe:GO/Fe(TMEDA):GO to 0.45–0.54 S cm^{-1} for Fe:rGO/Fe(TMEDA):rGO. Moreover, this 10^5-fold enhancement of electric conductivity for Fe:rGO/Fe(TMEDA):rGO enabled the rGO supporting materials to serve as a magneto-sensitizer for responsive generation of AMF-induced electric current and voltage, which were synchronized with the ON/OFF-switch for external application of AMF. Of interest, increase of AMF power from 0.64 kW to 2.24 kW induced elevation of (a) AMF-induced electric current from 151.8 ± 5.0/147.2 ± 3.9 μA to 610.3 ± 77.5/623.5 ± 26.0 μA and (b) AMF-induced electric voltage from 0.19/0.23 V to 0.62/0.95 V for Fe:rGO/Fe(TMEDA):rGO. That is, AMF

Open Access Article. Published on 03 November 2025. Downloaded on 4/1/2026 3:19:42 PM. This article is licensed under a Creative Commons Attribution-NonCommercial 3.0 Unported Licence.

power can serve as a remote control to tune the strength of magneto-driven electric current and voltage.

3. Upon application of AMF to H_2O_2 and FeSA:rGO, concomitant evolution of O_2 and formation of $^{\bullet}OH$ species occurred accompanied by decomposition of H_2O_2. In the absence of AMF, in contrast, the reaction of H_2O_2 and FeSA:rGO resulted in no oxygen evolution reaction and retarded degradation of H_2O_2. In addition, absent/limited decomposition of H_2O_2 was observed during the reaction of H_2O_2 and rGO under AMF. That is, using (a) electrically conductive rGO as a magneto-sensitizer for AMF-to-electricity conversion and (b) single-atom Fe as a catalytic active site, FeSA:rGO was developed as a magneto-catalyst for coupled oxidation of H_2O_2 into O_2 and reduction of H_2O_2 into $^{\bullet}OH/H_2O$. Based on the energy band diagram of FeSA:rGO, application of AMF was proposed to trigger a charge separation process leading to formation of low-lying electron holes at 2.41/2.43 eV *vs.* SHE, which promoted oxidation of the Fe^{3+} resting state and transient formation of high-valent Fe^{4+} species for oxidation of H_2O_2 into O_2. Meanwhile, the AMF-induced excited electrons at an energy level of −0.65/-0.57 eV *vs.* SHE provided a reduction power for Fe-mediated one-electron reduction of H_2O_2 into $^{\bullet}OH$ and H_2O (E° = 0.87 V for $H_2O_2 + H^+ + e^- \rightarrow H_2O + {}^{\bullet}OH$) or for Fe-mediated two-electron reduction of H_2O_2 into H_2O (E° = 1.76 V for $H_2O_2 + 2H^+ + 2e^- \rightarrow 2H_2O$).

Considering the abnormally high H_2O_2:O_2 ratio in the tumor, inflammatory, and injured tissue microenvironments, the integration of magneto-sensitizer and magneto-catalytic FeSA:rGO with biocompatible scaffold materials, such as the thermo-responsive poly(*N*-isopropylacrylamide) (PNIPAAM) hydrogel, held the potential for improving the biocompatibility of FeSA:rGO. In combination with tissue-penetrating AMF, the synchronized magneto-catalytic degradation of H_2O_2 and evolution of O_2 facilitated by FeSA:rGO can effectively reverse the hypoxic tumor microenvironment, thereby enhancing its anti-cancer and anti-inflammatory efficacy. Furthermore, the AMF-induced electric current and magneto-voltaic activity of FeSA:rGO provided a promising approach for inducing magneto-electric stimulation and promoting subsequent tissue repair and regeneration.[92,93] In addition to the *in vitro* and *in vivo* applications discussed above, applications of AMF and other types of varying magnetic fields to a series of molecular/colloidal/two-dimensional material/bulk magneto-sensitizer equipped with alternative catalytic active sites for magneto-catalysis will be explored in the near future.

Experimental section

Materials

Ammonium iron(II) sulfate hexahydrate ($Fe(NH_4)_2(SO_4)_2\cdot 6H_2O$, 99%, SHOWA), benzoic acid (99.5%, Alfa Aesar), deuterium oxide (D_2O, 99.9%, Sigma-Aldrich), dimethylformamide (DMF, 99.5% HPLC grade, Fisher Scientific), D-sorbitol (97%, VETEC), 5,5-dimethyl-1-pyrroline *N*-oxide (DMPO, >97.0%, TCI), glutathione (GSH, 98%, ACROS), graphite flakes (99.8%, Alfa Aesar), hydrogen peroxide (H_2O_2, >28%, UNION CHEMICAL), hydrochloric acid (HCl, UNION CHEMICAL), sodium L-lactate (98%, Sigma), methylene blue (>82%, Sigma-Aldrich), phenol (99%, Seedchem), potassium permanganate ($KMnO_4$, 99%, SHOWA), potassium phosphate dibasic (K_2HPO_4, 99%, AENCORE), potassium phosphate monobasic (KH_2PO_4, 99.5%, SHOWA), styrene oxide (98%, thermo scientific), sulfuric acid (H_2SO_4, 95+%, UNION CHEMICAL), and xylenol orange tetrasodium salt (ACROS) were used as received without further purification. Manipulations, reactions, and transfers were conducted under $N_{2(g)}$ according to Schlenk techniques. Organic solvents were distilled under $N_{2(g)}$ from appropriate drying agents (*n*-hexane and tetrahydrofuran (THF) from sodium/benzophenone) and stored in dried, $N_{2(g)}$-filled flasks over 4 Å molecular sieves. $N_{2(g)}$ was purged through these solvents before use. Complexes [Na-18-crown-6-ether][$(NO)_2Fe(\eta^2\text{-}BH_4)$] (**DNIC-BH$_4$**), [$(NO)_2$-Fe(TMEDA)] (TMEDA = tetramethylethylenediamine, **DNIC-TMEDA**), and [$(NO)_2Fe(\mu\text{-}SEt)_2Fe(NO)_2$] (**DNIC-SEt**) were prepared according to the reported procedures.[94–96] Preparation of Pt:rGO through coating of platinum on rGO was carried out with an ion sputtering device (E-1030, Hitachi High-Tech Corporation, Tokyo, Japan).

Instruments

Fourier-transform infrared (FT-IR) spectra were recorded on a PerkinElmer Spectrum Two spectrophotometer with sealed solution cells (0.1 mm, CaF_2 windows) or pressed KBr pellets. Detection of gaseous products (*i.e.* $H_{2(g)}$, $NO_{(g)}$, $N_2O_{(g)}$, and $O_{2(g)}$) during the preparation of FeSA:GO or application of AMF to the aqueous solution of H_2O_2 and FeSA:rGO was carried out using gas chromatography (GC, Shimadzu GC-2030 gas chromatograph equipped with a BID detector), where $He_{(g)}$ was adopted as the carrier gas. The ^{1}H NMR spectrum of the D_2O solution derived from extraction of Fe(TMEDA):GO, using 1*H*-pyrazole as an internal standard, was obtained on an Ascend 500 MHz spectrometer (AVANCE 500 NMR, BRUKER). For statistical evaluation of synthetic reproducibility, the average Fe contents of the as-prepared FeSA:GO, as-prepared FeSA:rGO, and used Fe:rGO were measured from three independently prepared batches. All Fe content values represented mean ± SD, with deviations within experimental error (±0.7 wt%). Each sample was digested in concentrated H_2SO_4 for 4 days and subsequently analyzed using an inductively coupled plasma optical emission spectrometer (ICP-OES, Agilent 725, US). UV-vis spectra were recorded on a PerkinElmer Lambda 365.

Powder X-ray diffraction (PXRD) patterns of GO, rGO, FeSA:GO, and FeSA:rGO were recorded with an X-ray diffractometer (Bruker D2 Phaser) using Cu K_α radiation (λ = 1.5418 Å). X-ray photoelectron spectroscopy (XPS) measurements of GO, rGO, FeSA:GO, and FeSA:rGO were conducted on PHI 5000 Versaprobe II and III (ULVAC-PHI, Japan) with a monochromatic Al anode as the X-ray source. To investigate the morphologies of GO, rGO, FeSA:GO, and as-prepared/used FeSA:rGO, powders of these materials were dispersed in ethanol and drop cast onto a Cu grid with carbon lacey. Then, the TEM/HRTEM/HAADF-STEM images and corresponding EDS mappings were acquired at 200 kV with a spherical aberration corrector (JEOL JEM-ARM200FTH). The single-atom Fe images of FeSA:GO and

© 2026 The Author(s). Published by the Royal Society of Chemistry

Open Access Article. Published on 03 November 2025. Downloaded on 4/1/2026 3:19:42 PM. This article is licensed under a Creative Commons Attribution-NonCommercial 3.0 Unported Licence.

FeSA:rGO were acquired on a STEM attachment coupled to an HRTEM (JEOL JEM-ARM200FTH). Furthermore, the profile function in Gatan DigitalMicrograph software was utilized to extract intensity profiles from three distinct regions of each sample in order to measure the distances between adjacent single-atom Fe atoms. Electric conductivities of GO, rGO, FeSA:GO, and FeSA:rGO were determined using a four-point probe measurement system (Sadhudesign, Taiwan). UV-vis diffuse reflectance spectra of FeSA:rGO were recorded using a JASCO V-670 spectrophotometer equipped with an integrating sphere. Using a conventional 3-electrode system coupled to a Zahner Zennium E workstation, cyclic voltammetry (CV) measurements were performed to investigate the highest occupied molecular orbital (HOMO) of FeSA:rGO. 1 mL of an ethanol solution of FeSA:rGO (1 mg mL^{-1}) was deposited on a FTO substrate, which was used as the working electrode. On the other hand, a platinum wire and an Ag/AgCl electrode were used as the counter electrode and the reference electrode, respectively. A cyclic voltammogram was obtained in CH_3CN containing 0.1 M tetrabutylammonium perchlorate as electrolyte.

Mössbauer measurements

Using a SeeCo constant acceleration spectrometer equipped with a temperature controller maintaining temperatures within ±0.1 K and a ^{57}Co radiation source in a Rh matrix, zero-field ^{57}Fe Mössbauer spectra of FeSA:GO and FeSA:rGO were recorded at 80 K. All measurements were performed under an $N_{2(g)}$ atmosphere. Isomer shifts are referred to as α-Fe metal at room temperature. Data were fitted with a sum of Lorentzian quadrupole doublets by using a least-squares routine with the WMOSS program.[97]

Fe K-edge X-ray absorption near-edge spectroscopy (XANES) and extended X-ray absorption fine structure (EXAFS)

The X-ray absorption experiment was carried out at the National Synchrotron Radiation Research Center (NSRRC), Hsinchu, Taiwan. Samples were ground to powder and secured in a bag made of 6 μm Mylar film. The Fe K-edge X-ray absorption near-edge spectroscopy (XANES) data of FeSA:GO and as-prepared/used FeSA:rGO were collected in fluorescence mode at BL 16A and BL 17C using a Si (111) double-crystal monochromator. A Lytle detector was employed for fluorescence measurements in which the sample chamber is filled with high-purity He gas to avoid air absorption. The photon energy was calibrated to the maximum of the first inflection point at 7112.0 eV of the Fe foil spectrum. The acquired data were extracted and processed with Athena and Artemis implemented in IFEFFIT version 0.9.26. For statistical reproducibility, data of the FeSA:GO and as-prepared/used FeSA:rGO samples from three independently prepared batches exhibiting consistent spectral features were averaged using the Athena software. Then, a smooth background was removed from all spectra by fitting a straight line to the pre-edge region and subtracting this straight line from the entire spectrum. Normalization of the data was accomplished by fitting a flat polynomial to the post-edge region and normalizing the edge jump to 1.0.

Subsequently, k^3-weighted $\chi(k)$ data in the k-space were Fourier transformed to real (R) space by means of a hanning window ($dk = 1.0$ Å^{-1}) to evaluate the EXAFS contributions from different coordination shells. Moreover, Fourier transformed fittings were performed to obtain the quantitative structural parameters around the central Fe atom in Artemis. The models including monodentate carboxylate, bidentate carboxylate, and bidentate tetramethylethylenediamine were used to calculate the simulated scattering paths. The passive electron reduction factor (S_0^2), energy shift (ΔE_0), bond length (R), and Debye–Waller factor (σ^2) were allowed to run freely. Wavelet transform plots were depicted from the k^3-weighted $\chi(k)$ data exported from Athena, followed by the computation using the Morlet function with $\kappa = 7$ and $\sigma = 1$ to provide the overall distribution.

Preparation and characterization of graphene oxide (GO)

Graphene oxide was synthesized based on a modified Hummers' method.[98] In a 100 mL serum bottle containing 40 mL of concentrated sulfuric acid, 3 g of graphite flakes and 1 g of $KMnO_4$ were added. After this, the mixture reaction solution was stirred in an ice bath for 5 min, the ice bath was removed, and the mixture reaction solution was stirred at 40 °C for 2 h to obtain a dark-green viscous solution. Subsequently, the obtained dark-green viscous solution was poured into a beaker loaded with 300 mL of icy ddH_2O followed by addition of 5 mL of $H_2O_{2(aq)}$ in a dropwise manner. The obtained bright-yellow solution was kept undisturbed overnight and centrifuged at 6000 rpm for 10 min before the supernatant solution was removed and the precipitates were washed with 50 mL of 10% $HCl_{(aq)}$. After the precipitates were washed with 50 mL ddH_2O 5 times, lyophilization of the washed graphene oxide at −50 °C for 1 day was performed to yield graphene oxide as a black powder (yield 1.7 g).

Based on the reported literature,[98] sequential reaction of graphite with $KMnO_4$ and H_2O_2 was performed to prepare graphene oxide (GO). As shown in SI Fig. 1a, IR absorption peaks at 1732, 1622, 1416/1169/596, and 1040 cm^{-1} are assigned to the vibrational features for C=O, C=C, O–H, and C–O–C groups, respectively, derived from carboxylic acid, phenol, and epoxide functional groups on GO.[99–101] In addition, the powder X-ray diffraction peak at 2θ = 9.4°, C 1s peaks at (284.2, 286.4, 287.6) eV, and O_{1s} peaks at (531.6, 532.3, 533.5) eV revealed by powder X-ray diffraction (PXRD) and X-ray photoelectron spectroscopy (XPS) analyses supported the successful synthesis of GO (SI Fig. 5a–b).[102,103]

Reactivity study of GO toward complex [Na-18-crown-6-ether][$(NO)_2Fe(\eta^2\text{-}BH_4)$] (or complex [$(NO)_2Fe$(TMEDA)]) leading to the formation of Fe:GO (or Fe(TMEDA):GO)

To a 20 mL Schlenk tube loaded with 0.1 mmol of [Na-18-crown-6-ether][$(NO)_2Fe(\eta^2\text{-}BH_4)$] (**DNIC-BH$_4$**) and 200 mg of GO, 10 mL of THF was added *via* stainless cannula under positive $N_{2(g)}$ pressure at room temperature. This mixture reaction solution was stirred for 6 h and then monitored by FT-IR, disappearance of IR ν_{NO} stretching frequencies at 1708 and 1654 cm^{-1} suggested the complete degradation of **DNIC-BH$_4$**. On the other

Open Access Article. Published on 03 November 2025. Downloaded on 4/1/2026 3:19:42 PM. This article is licensed under a Creative Commons Attribution-NonCommercial 3.0 Unported Licence.

hand, analysis of the gaseous product(s) in the headspace using GC revealed evolution of $H_{2(g)}/N_2O_{(g)}$ and no formation of $NO_{(g)}$. After this, the mixture reaction solution was transferred to a 15 mL centrifuge tube filled with $N_{2(g)}$ *via* stainless cannula and centrifuged at 10 000 rpm for 10 min, the supernatant THF solution was transferred to another Schlenk tube filled with $N_{2(g)}$ before the residual black precipitates were washed with THF twice and dried under vacuum (yield 0.18 g, denoted as Fe:GO). To characterize the potential formation of NO_2^-/NO_3^- in the prepared Fe:GO, the as-prepared Fe:GO was incubated in 1 M $NaOH_{(aq)}$ for 2 days before analysis of the supernatant aqueous solution using the Nitrate/Nitrite Colorimetric Assay Kit (Item No. 780001, Cayman), which indicated no formation of NO_2^-/NO_3^-. On the other hand, potential formation of NO_2^-/NO_3^- in the collected supernatant THF solution was examined using the Nitrate/Nitrite Colorimetric Assay Kit (Item No. 780001, Cayman), which indicated the negligible formation of NO_2^-/NO_3^-.

Upon reaction of **DNIC-BH$_4$** (0.1 mmol) with GO (200 mg) in THF under an $N_{2(g)}$ atmosphere for 6 h, disappearance of the brown color and indicative IR ν_{NO} features (1708 and 1654 cm^{-1}) for **DNIC-BH$_4$** in the THF supernatant solution occurred accompanied by the formation of an IR absorption peak at 2223 cm^{-1} (SI Fig. 1b). In comparison with the solid-state IR spectra of the as-prepared GO and **DNIC-BH$_4$**, the absence of IR ν_{NO} features in the 1708 and 1654 cm^{-1} was observed in the IR spectrum for the GO treated with **DNIC-BH$_4$** (SI Fig. 1 and 2). Accordingly, GO promoted the decomposition of the dinitrosyl iron unit (DNIU) $[Fe(NO)_2]$ in **DNIC-BH$_4$** and evolution of $N_2O_{(g)}$, while limited formation of NO_2^-/NO_3^- in the THF supernatant solution and absence of evolution of $NO_{(g)}$ in the headspace was confirmed using a total nitrate/nitrite assay kit and gas chromatography (GC, SI Fig. 1d), respectively. As shown in SI Fig. 1a, d, and 2, absence of IR ν_{B-H} features in the 1800–2500 cm^{-1} region exhibited by **DNIC-BH$_4$**-treated GO and formation of $H_{2(g)}$ in the headspace for the reaction between **DNIC-BH$_4$** and GO suggested the acid–base reaction between the carboxylic acid/phenol groups of GO with the $[BH_4]^-$ in **DNIC-BH$_4$**.

After the GO-induced transformation of **DNIC-BH$_4$**, the retained IR absorption peaks at 1730, 1141, and 1076 cm^{-1} exhibited by the **DNIC-BH$_4$**-treated GO resembled IR features derived from the carboxylic acid, phenol, and epoxide functional groups on the as-prepared GO (SI Fig. 1a). Moreover, the Fe content in the **DNIC-BH$_4$**-treated GO is further determined as 2.5 ± 0.7 wt% based on the ICP-OES analysis, which is comparable to the theoretical Fe content (2.8 wt%) considering the complete deposition of Fe from **DNIC-BH$_4$** onto GO. Upon extraction of **DNIC-BH$_4$**-treated GO with 1 M $NaOH_{(aq)}$, absence of NO_2^- and NO_3^- was validated using a total nitrate/nitrite assay kit. That is, the carboxylic acid/phenol functional groups on GO, presumably, induced the protonation of Fe-bound $[BH_4]^-$, conversion of Fe-bound NO into $N_2O_{(g)}$, and deposition of Fe on GO leading to the assembly of Fe:GO.

Reaction of $[(NO)_2Fe(TMEDA)]$ (TMEDA = tetramethylethylenediamine, **DNIC-TMEDA**) with GO, characterization of **DNIC-TMEDA**-treated GO (denoted as Fe(TMEDA):GO), and analyses of the accompanied byproducts were performed under a similar procedure. In addition, after extraction of the prepared Fe(TMEDA):GO with 1 M NaOD in D_2O for 2 days, ^1H NMR analysis of the signals at 2.259 and 1.998 ppm, using 1H-pyrazole (37 mM) as an internal standard, was performed to determine the amount of TMEDA on the prepared Fe(TMEDA):GO.

Reaction of **DNIC-TMEDA** (0.1 mmol) with GO (200 mg) followed by characterization of **DNIC-TMEDA**-treated GO was carried out in a similar manner. Similar to the reaction between **DNIC-BH$_4$** and GO, GO-induced transformation of **DNIC-TMEDA** and deposition of Fe on **DNIC-TMEDA**-treated GO (Fe content = 1.6 ± 0.1 wt%) were explored based on the solid-state/solution IR study, total nitrate/nitrite assay, and ICP-OES analysis (SI Fig. 1a and c). During the reaction between **DNIC-TMEDA** and GO, of interest, GC analysis of the gaseous sample in the headspace revealed the absence of $H_{2(g)}$ and evolution of $NO_{(g)}$ (SI Fig. 1d), in addition to the generation of $N_2O_{(g)}$ according to the distinctive IR absorption peak at 2223 cm^{-1}. After extraction of **DNIC-TMEDA**-treated GO with 1 M NaOD in D_2O, formation of 1.8 ± 0.6 wt% of Fe-bound TMEDA on GO was determined based on the ^1H NMR signal at 2.259 and 1.998 ppm (SI Fig. 3). This quantitation of Fe and TMEDA on **DNIC-TMEDA**-treated GO reflected an Fe:TMEDA ratio of ~1.125:1. Based on the investigations described above, the different supporting ligands in Fe precursors, namely **DNIC-BH$_4$** and **DNIC-TMEDA**, control the buildup of Fe:GO and Fe(TMEDA):GO, respectively, through distinctive transformation/deposition mechanisms.

Reaction of complex $[(NO)_2Fe(\mu\text{-}SEt)_2Fe(NO)_2]$ and GO

Reaction of complex $[(NO)_2Fe(\mu\text{-}SEt)_2Fe(NO)_2]$ (**DNIC-SEt**) (0.017 g, 0.05 mmol) and GO (200 mg) was performed under a procedure similar to the reaction of GO with **DNIC-BH$_4$** (or **DNIC-TMEDA**) described above. As opposed to **DNIC-BH$_4$** and **DNIC-TMEDA**, **DNIC-SEt** features an inert nature toward GO according to the unchanged IR ν_{NO} absorption peaks at 1774 and 1749 cm^{-1} observed after its reaction with GO for 8 h (SI Fig. 4). This inert nature of **DNIC-SEt** toward GO, moreover, echoed the critical role of supporting ligands in Fe precursors in the fabrication of single-atom Fe on the GO supporting materials.

Characterization of GO, Fe:GO, and Fe(TMEDA):GO by XPS

X-ray photoelectron spectroscopy (XPS) measurements of GO, Fe:GO, and Fe(TMEDA):GO were conducted on PHI 5000 Versaprobe II and III (ULVAC-PHI, Japan) with a monochromatic Al anode as the X-ray source. XPS C 1s and O 1s spectra of GO, Fe:GO, and Fe(TMEDA):GO were depicted in SI Fig. 5b–d. The strong carbon peaks at 284.2–284.4 eV and 286.4–286.7 eV corresponded to the C=C functional groups derived from the original graphite precursor and dominant formation of oxygenated C–OH/C–O–C functional groups, respectively, whereas the shoulder carbon peaks at 287.6–288.3 eV indicated the minor formation of C=O functional groups.[104,105] On the other hand, the oxygen peaks at 531.6–531.8 eV, 532.3–532.7 eV,

© 2026 The Author(s). Published by the Royal Society of Chemistry

Open Access Article. Published on 03 November 2025. Downloaded on 4/1/2026 3:19:42 PM.
This article is licensed under a Creative Commons Attribution-NonCommercial 3.0 Unported Licence.

and 533.5–534.7 eV corresponded to O–C═O, C═O, and C–OH/C–O–C functional groups, respectively.[103] These XPS C 1s and O 1s spectra of GO supported the successful oxidation of graphite and incorporation of carboxylic acid, phenol, and epoxide functional groups in GO. On the other hand, the C 1s and O 1s spectra of both Fe:GO and Fe(TMEDA):GO are comparable to those of the as-prepared GO. As shown in SI Fig. 5c and d, the two peaks at 712.2 eV and 725.4 eV (or 712.6 eV and 725.8 eV) were assigned to Fe $2p_{3/2}$ and Fe $2p_{1/2}$ for the Fe^{3+} center in Fe:GO (or Fe(TMEDA):GO).[106] These weak Fe 2p features displayed by Fe:GO and Fe(TMEDA):GO may be ascribed to the limited Fe content.

XANES study of Fe:GO, Fe(TMEDA):GO, $Fe^{II}Pc$, and $Fe^{III}TPPCl$

Normalized Fe K-edge XANES spectra for Fe:GO and Fe(TMEDA):GO as well as two reference complexes $Fe^{II}Pc$ (*Pc* = phthalocyanine) and $Fe^{III}TPPCl$ (TPP = tetraphenylporphyrin) were included in Fig. 3a in the main text. In comparison with the $Fe_{1s} \rightarrow Fe_{3d}$ pre-edge absorption peaks at 7114.2 eV and 7114.5 eV exhibited by $Fe^{II}Pc$ and $Fe^{III}TPPCl$, both Fe:GO and Fe(TMEDA):GO displayed $Fe_{1s} \rightarrow Fe_{3d}$ pre-edge absorption peaks at 7114.8 eV. Besides, the apparent intensity for the $Fe_{1s} \rightarrow Fe_{3d}$ pre-edge features followed the order of four-coordinate $Fe^{II}Pc$ > five-coordinate $Fe^{III}TPPCl$ > Fe:GO/Fe(TMEDA):GO. Of importance, the energy and apparent intensity of the $Fe_{1s} \rightarrow Fe_{3d}$ pre-edge absorption peaks supported that the single-atom Fe in both Fe:GO and Fe(TMEDA):GO was an O-/N-bound Fe^{3+} center embedded in an octahedral geometry.

Reactivity study of complex DNIC-BH4 (or DNIC-TMEDA) toward benzoic acid, phenol, and styrene oxide

To a 20 mL Schlenk tube loaded with **DNIC-BH_4** (0.418 g, 0.1 mmol) and benzoic acid (0.112 g, 0.1 mmol), 8 mL of THF was added *via* stainless cannula under positive $N_{2(g)}$ pressure at room temperature. After this, the reaction solution was stirred at ambient temperature for 1 day, and the disappearance of IR ν_{NO} stretching frequencies at 1708 cm^{-1} and 1654 cm^{-1} suggested the complete degradation of **DNIC-BH_4**. Reactions of **DNIC-BH_4** with phenol/styrene oxide in a 1:1 stoichiometry and reactions of **DNIC-TMEDA** with benzoic acid/phenol/styrene oxide in a 1:1 stoichiometry were performed under a similar procedure. Degradation of **DNIC-BH_4** upon reaction with phenol and decomposition of **DNIC-TMEDA** during reaction with benzoic acid were observed based on the disappearance of distinctive IR ν_{NO} features. In comparison, no reaction was observed during reaction of **DNIC-BH_4** with styrene oxide or reaction of **DNIC-TMEDA** with phenol/styrene oxide.

Considering the presence of carboxylic acid, phenol, and epoxide functional groups on the as-prepared GO, reactions of **DNIC-BH_4**/**DNIC-TMEDA** with benzoic acid, phenol, and styrene oxide were investigated in an attempt to depict the mechanisms for reaction between GO and **DNIC-BH_4** or **DNIC-TMEDA**. Based on the IR spectroscopic study shown in SI Fig. 9 and 10, benzoic acid and phenol exhibited the reactivity to promote the transformation/decomposition of **DNIC-BH_4**, while **DNIC-TMEDA** was reactive toward benzoic acid instead of phenol and styrene oxide.

Preparation of reduced graphene oxide (rGO) and FeSA:rGO (Fe:rGO and Fe(TMEDA):rGO)

Preparation of rGO was carried out based on a reported one-step solvothermal reduction approach.[107] 30 mg of the as-prepared GO was dispersed in 60 mL of DMF and this DMF solution of GO was stirred in an oil bath at 155 °C for 2 h. After this, the DMF reaction solution was cooled down to room temperature and centrifuged at 10 000 rpm for 10 min, the supernatant solution was removed before the precipitated reduced GO (rGO) was washed with DMF and dried at 80 °C in an oven (yield 9 mg). Preparations of Fe:rGO (yield 13 mg) and Fe(TMEDA):rGO (yield 11 mg) were performed under a similar procedure using Fe:GO and Fe(TMEDA):GO, respectively, as the precursor.

Characterizations of rGO, Fe:rGO, and Fe(TMEDA):rGO by XPS and solid-state IR spectroscopy

X-ray photoelectron spectroscopy (XPS) measurements of rGO, Fe:rGO, and Fe(TMEDA):rGO were conducted on PHI 5000 Versaprobe II and III (ULVAC-PHI, Japan) with a monochromatic Al anode as the X-ray source. During the conversion of Fe:GO/Fe(TMEDA):GO into Fe:rGO/Fe(TMEDA):rGO, reduction of GO_{phenol}/$GO_{epoxide}$ and transformation of $GO_{carboxylic\ acid}$ into GO_{amide} was evidenced by XPS and solid-state IR spectroscopy (SI Fig. 14 and 15).[108] In comparison with GO/Fe:GO/Fe(TMEDA):GO, in addition to the retained XPS C 1s peak at 284.5 eV corresponding to the C═C group, a significant reduction of the XPS C 1s peaks at 286.1–286.8 eV, which was indicative of the C–OH/C–O–C groups, was observed.[109,110] During the solvothermal process at 155 °C, degradation of DMF was reported to yield dimethylamine and CO, which served as a reductant to eliminate the C–OH and C–O–C functional groups.[111,112] Meanwhile, the predominant XPS N 1s peaks at 401.6–401.8 eV and XPS O 1s peaks at 531.5–531.8 eV are assigned to the O═C–N amide group (SI Fig. 14a–c), while the predominant XPS N 1s peaks at 399.8–399.9 eV are assigned to the C–N group.[113,114] As shown in SI Fig. 14d, the electronic structure of the single-atom Fe in Fe:rGO/Fe(TMEDA):rGO is best described as Fe^{3+} according to the XPS Fe $2p_{3/2}$ and Fe $2p_{1/2}$ peaks at 712.6/711.6 eV and 725.5/725.4 eV, respectively.

Measurement of alternating magnetic field (AMF)-induced current and voltage

To investigate the AMF-induced electric current and voltage, GO (14.8 mg)/rGO (14.0 mg)/FeSA:GO (13.6 mg)/FeSA:rGO (8.5 mg) was pressed into a pellet with a diameter of 1 cm and a thickness below 1 mm using a manual hydraulic press. After the pellet of GO/rGO/FeSA:GO/FeSA:rGO was placed in a homemade acrylic holder located 1 cm below the 1.1 cm solenoid coil, 20%/50%/70% power intensity of AMF (P = 0.64/1.6/2.24 kW, B = 1.58/3.95/5.53 mT) generated by a high frequency generator (Power Cube 32/900) was applied to the pellet of GO/rGO/FeSA:GO/FeSA:rGO. Under the application of AMF, the pellet of GO/rGO/FeSA:GO/FeSA:rGO was connected to a digital

Open Access Article. Published on 03 November 2025. Downloaded on 4/1/2026 3:19:42 PM. This article is licensed under a Creative Commons Attribution-NonCommercial 3.0 Unported Licence.

bench oscillator (Tektronix MSO44 4-BW-350, 4 Series MSO Mixed Signal Oscilloscope, 4 Channel, 350 MHz) through copper wires in order to measure the voltage–time (*V*–*t*) curves, whereas a digital multimeter (PROVA 803) was utilized to measure the current–time (*I*–*t*) curves (SI Fig. 19b and c). All the *V*–*t* curves were further processed using Fast Fourier Transform (FFT), Inverse Fast Fourier Transform (IFFT), and Cosine Fitting (COSFIT) embedded in the MATLAB software to obtain the AMF-induced electric voltage.

Elimination of hydrogen peroxide by FeSA:GO (or FeSA:rGO) with/without application of AMF

In a 2 mL Eppendorf tube, 2 mg of FeSA:rGO (Fe:rGO or Fe(TMEDA):rGO) was suspended in 2 mL of 50 mM phosphate buffer (pH 6.5) containing 100 μM (or 500 μM) H_2O_2 and treated with AMF at a 50% power intensity (1.6 cm coil, 1.6 kW, 3.75 mT). After application of AMF for 20, 40, 60, 90, 120, and 180 min, respectively, a 50 μL aliquot of this mixture solution was collected and mixed with 950 μL of colorimetric Fox reagent, which was an aqueous solution containing ferrous ammonium sulfate (0.25 mM), D-sorbitol (100 mM), xylenol orange tetrasodium salt (0.08 mM), and sulfuric acid (26.3 mM).[115] After reaction with the colorimetric Fox reagent for 15 min, the absorbance at 560 nm was recorded using UV-vis spectroscopy and adopted to quantify the concentration of H_2O_2. Three independent experiments were conducted to obtain an average curve for time-dependent consumption of H_2O_2 by FeSA:rGO under AMF. Elimination of hydrogen peroxide by FeSA:GO and FeSA:rGO in the absence of AMF was performed in a similar manner. During the reaction of FeSA:rGO and H_2O_2 in the absence of AMF, analysis of the gaseous product in the headspace using GC revealed enhanced evolution of $CO_{2(g)}$, while the H_2O_2-treated FeSA:rGO was collected and analyzed using XPS.

Generation of dioxygen derived from elimination of hydrogen peroxide by FeSA:rGO with/without application of AMF

To a $N_{2(g)}$-filled 20 mL glass tube loaded with 3 mg of FeSA:rGO (Fe:rGO or Fe(TMEDA):rGO), anaerobic 50 mM phosphate buffer (pH 6.5) containing 100 μM H_2O_2 (or 500 μM H_2O_2) was added before the dissolved oxygen probe (edge DO HI764080) of a dissolved oxygen meter (edge DO HI2004) was inserted into this tube and immersed into this aqueous solution. Subsequently, this tube was sealed under $N_{2(g)}$ and placed in the middle of the solenoid soil (1.6 cm coil). Upon application of AMF to the aqueous solution of FeSA:rGO and H_2O_2 at a power intensity of 50% (1.6 kW, 3.75 mT), evolution of $O_{2(g)}$ dissolved in this aqueous solution was recorded every 5 min for 3 h using a dissolved oxygen meter. Three independent experiments were conducted to obtain an average curve for time-dependent generation of O_2 by FeSA:rGO under AMF, and data were presented as mean ± SD. Time-dependent O_2-evolution profiles catalyzed by FeSA:rGO were measured in 50 mM phosphate buffer (pH 5.5, 6.5, or 7.4) with or without AMF, and in the presence or absence of 1 mM glutathione (GSH) or 10 mM lactate, following the same procedure described above. On the other hand, using a Shimadzu GC-2030 gas chromatograph equipped with a BID detector, analysis of the gaseous product from the headspace of the aqueous solution of H_2O_2 (500 μM) and Fe:rGO (1 mg mL^{-1}, or Fe(TMEDA):rGO (1 mg mL^{-1})) under AMF also supported time-dependent generation of O_2 (SI Fig. 21).

Evaluation of FeSA:rGO recyclability

To evaluate the recyclability of Fe:rGO (or Fe(TMEDA):rGO) for magneto-catalytic OER, seven (or five) consecutive cycles of AMF application to an aqueous solution containing 1 mg mL^{-1} Fe:rGO (or 1 mg mL^{-1} Fe(TMEDA):rGO) and 500 μM H_2O_2 at a power intensity of 50% (1.6 kW, 3.75 mT) were performed. Each experiment was conducted in triplicate. Following the procedure described above, the magneto-catalytic evolution of O_2 during each cycle was monitored using a dissolved oxygen probe in conjunction with a dissolved oxygen meter. After each magneto-catalytic OER cycle, the suspension solution was centrifuged at 10 000 rpm for 10 min to remove (or to collect) the supernatant solution. Then, the recovered Fe:rGO (or Fe(TMEDA):rGO) was reused in the subsequent magneto-catalytic OER cycle or subjected to further characterization by HRTEM, HAADF-STEM, XANES, EXAFS, and ICP-OES following the procedure described in the Instruments and Fe K-edge X-ray Absorption Near-edge Spectroscopy (XANES) and Extended X-ray Absorption Fine Structure (EXAFS) sections.

Kinetic study of magneto-catalytic evolution of O_2 promoted by FeSA:rGO

The dependence of the magneto-catalytic O_2 evolution rate on (a) FeSA:rGO concentration, (b) H_2O_2 concentration, and (c) AMF power intensity was investigated to elucidate the mechanism of magneto-catalytic O_2 evolution promoted by FeSA:rGO. A nitrogen-filled ($N_{2(g)}$) 20 mL glass tube was loaded with Fe:rGO (or Fe(TMEDA):rGO) at concentrations of 0.25 mg mL^{-1}, 0.5 mg mL^{-1}, 0.75 mg mL^{-1}, or 1 mg mL^{-1} in anaerobic 50 mM phosphate buffer (pH 6.5) containing 750 μM H_2O_2. Then, a dissolved oxygen probe (edge DO HI764080) connected to a dissolved oxygen meter (edge DO HI2004) was inserted into this glass tube and immersed in the aqueous solution described above. Subsequently, this tube was then sealed under $N_{2(g)}$ and placed at the center of a solenoid coil (1.6 cm in diameter). Upon applying AMF at a power intensity of 50% (1.6 kW) to the aqueous solution of Fe:rGO (or Fe(TMEDA):rGO) and H_2O_2, the evolution of dissolved O_2 was recorded every 5 minutes for 3 hours using the dissolved oxygen meter. Three independent experiments were conducted to determine the average O_2 evolution rate and its standard deviation for the magneto-catalytic reaction promoted by Fe:rGO (or Fe(TMEDA):rGO).

Following a similar methodology, additional experiments were conducted under the following conditions:

(a) AMF at a power intensity of 50% (1.6 kW) was applied to a solution containing 1 mg mL^{-1} Fe:rGO (or Fe(TMEDA):rGO) and H_2O_2 at concentrations of 100 μM, 250 μM, 500 μM, or 750 μM in anaerobic 50 mM phosphate buffer (pH 6.5).

(b) AMF at power intensities of 0%, 10% (0.32 kW), or 30% (0.96 kW) was applied to a solution containing 1 mg mL^{-1}

© 2026 The Author(s). Published by the Royal Society of Chemistry

Open Access Article. Published on 03 November 2025. Downloaded on 4/1/2026 3:19:42 PM. This article is licensed under a Creative Commons Attribution-NonCommercial 3.0 Unported Licence.

Fe:rGO (or Fe(TMEDA):rGO) and 500 μM H_2O_2 in anaerobic 50 mM phosphate buffer (pH 6.5).

(c) AMF at a power intensity of 50% (1.6 kW) was applied to a 9 mL solution containing 750 μM H_2O_2 and Fe(TMEDA):rGO (1 mg mL^{-1} as well-dispersed powder or 9 mg as a bulk pellet) in anaerobic 50 mM phosphate buffer (pH 6.5).

Generation of a H_2O_2-derived hydroxyl radical by FeSA:rGO with/without application of AMF

Transient generation of hydroxyl radicals during the reaction of H_2O_2 and FeSA:rGO with/without application of AMF was monitored using a methylene blue (MB)-based colorimetric assay and using 5,5-dimethyl-1-pyrroline *N*-oxide (DMPO) as a radical spin trapping agent. In a 2 mL Eppendorf tube, 2 mg of Fe:rGO (or Fe(TMEDA):rGO) was suspended in 2 mL of 50 mM potassium phosphate buffer (pH 6.5) containing 100 μM H_2O_2. Then, 40 μL of 5 mM $MB_{(aq)}$ was added into this mixture solution before external application of AMF at a 50% power intensity (1.6 cm coil, 1.6 kW, 3.75 mT). After application of AMF for 0, 20, 60, 120, and 180 min, respectively, this mixture solution was centrifuged at 10 000 rpm for 30 s A 70 μL aliquot of this supernatant solution was added into 490 μL of 50 mM potassium phosphate buffer (pH 6.5) before the UV-vis spectrum of this diluted solution was measured. Time-dependent changes of the UV-vis spectra for (a) reaction of Fe:rGO (or Fe(TMEDA):rGO), H_2O_2 and MB and (b) reaction of H_2O_2 and MB in the absence of AMF were explored in a similar manner.

On the other hand, 100 μM H_2O_2 in 50 mM potassium phosphate buffer (pH 6.5, 3 mL) was added into a 15 mL centrifuge tube loaded with 3 mg of Fe:rGO (or Fe(TMEDA):rGO). After external application of AMF at 50% intensity (1.6 cm coil, 1.6 kW, 3.75 mT) for 20 min, this mixture solution was centrifuged at 10 000 rpm for 30 s A 990 μL aliquot of this supernatant solution was mixed with 10 μL of DMPO in an Eppendorf tube before the obtained mixture solution was transferred into the EPR quartz tube for EPR measurement. EPR spectra for (a) DMPO in 50 mM potassium phosphate buffer (pH 6.5), (b) reaction of H_2O_2 with DMPO, and (c) reaction of Fe:rGO (or Fe(TMEDA):rGO), H_2O_2, and DMPO in the absence of AMF were measured in a similar manner.

Characterization of magneto-catalytic reaction Intermediate(s) through freeze-quench experiments in combination with XANES, EPR, and Mössbauer spectroscopy

After a hole with a 4 mm diameter was created on the side of a 2 mL Eppendorf tube, this hole was covered with Kapton tape before this tube was loaded with 750 μM H_2O_2 and 50 mg mL^{-1} Fe:rGO (or Fe(TMEDA):rGO) in 50 mM phosphate buffer (pH 6.5). An AMF at a power intensity of 50% (1.6 kW) was applied to this aqueous solution of Fe:rGO (or Fe(TMEDA):rGO) and H_2O_2 for 1 min (or 0.5 min, this time point was chosen considering that the magneto-catalytic reactions are still undergoing). Then, this AMF-treated aqueous solution of Fe:rGO (or Fe(TMEDA):rGO) and H_2O_2, together with the tube, was incubated in $N_{2(l)}$ right away in order to freeze quench the magneto-catalytic reaction intermediate(s). The freeze-quenched magneto-catalytic reaction intermediate(s) was then stored in $N_{2(l)}$ before the subsequent XANES experiments. These samples were denoted as "FeSA:rGO under magneto-catalysis". On the other hand, after freezing the aqueous solution of FeSA:rGO without exposure to AMF, the samples obtained are denoted as "FeSA:rGO under resting state".

FQ-XANES measurements of FeSA:rGO under magneto-catalysis and FeSA:rGO in the resting state were collected at NSRRC TPS 32A. The samples were maintained at 100 K during data collection using an 800 Cryostream PLUS. A 19-channel silicon drift detector was employed for fluorescence measurements. All the other data acquisition and processing procedures are the same as those described in the Fe K-edge X-ray Absorption Near-edge Spectroscopy (XANES) and Extended X-ray Absorption Fine Structure (EXAFS) section. The Fe_{1s}-to-Fe_{3d} pre-edge features were fitted using the Athena software over the range of 7105–7120 eV.

In a similar manner, freeze-quenched samples were prepared through (a) application of AMF (1.6 kW) to an aqueous solution of Fe:rGO (10 mg mL^{-1}) and H_2O_2 (750 μM), loaded in a Mössbauer cup, for 10 min followed by a freeze-quenching process in $N_{2(l)}$ or (b) application of AMF (1.6 kW) to an aqueous solution of Fe:rGO/Fe(TMEDA):rGO (10 mg mL^{-1}) and H_2O_2 (750 μM), loaded in an EPR tube, for 5 min or 10 min followed by a freeze-quenching process in $N_{2(l)}$. Then, the Mössbauer and EPR spectra for these FQ samples were collected following the procedure described in the Mössbauer Measurements and X-band EPR Spectroscopy section.

X-band EPR spectroscopy

When using DMPO as a radical spin trapping agent, the EPR spectra were recorded at room temperature using a Bruker ELEXSYS-E580 spectrometer with a microwave power of ~15 mW, frequency of 9.83 GHz, sampling time of 20.4 ms, receiver gain of 30, and modulation amplitude of 1.6 mT at 100 kHz. For FeSA:rGO in the resting state and FeSA:rGO under magneto-catalysis, the EPR spectra were recorded on a Bruker EMX/Plus spectrometer (Billerica, MA), equipped with a dual-mode ER 4116DM cavity that supports both parallel (TE_{012}) and perpendicular (TE_{102}) modes of polarization of the applied magnetic field. Low temperature (4.7 K) was achieved and maintained with a liquid helium quartz cryostat (Oxford Instruments ESR900), complemented by a cryogenic temperature controller (Oxford Instruments mercuryiTC). The microwave frequency was set to 9.636 GHz for the perpendicular mode (TE_{102}) and 9.363 GHz for the parallel mode (TE_{012}), with a microwave power of 2.031 mW. Spectra were acquired using a magnetic field modulation frequency of 100 kHz and a modulation amplitude of 1 mT. Each spectrum was recorded with a digital field resolution of 0.5 mT/point.

Magnetothermal properties of Fe:rGO (or Fe(TMEDA):rGO) under AMF

A 20 mL glass tube was loaded with 2 mg of Fe:rGO (or Fe(TMEDA):rGO) and 2 mL of 100 μM $H_2O_{2(aq)}$. Using a cylindrical solenoid with a 1.6 cm diameter, an alternating magnetic field

Open Access Article. Published on 03 November 2025. Downloaded on 4/1/2026 3:19:42 PM. This article is licensed under a Creative Commons Attribution-NonCommercial 3.0 Unported Licence.

(AMF) at an output intensity of 1.60 kW (50%) was applied to this tube loaded with 1 mg mL^{-1} Fe:rGO (or Fe(TMEDA):rGO) in 100 μM $H_2O_{2(aq)}$. The temperature was recorded before and after application of AMF for 10 min using an IR thermal imaging camera (Thermo Shot F30S, NEC). Magnetothermal activity of Fe:rGO (or Fe(TMEDA):rGO) powder was measured in a similar manner.

Computational Methods and insights into the mechanism for catalytic conversion of H_2O_2 into O_2

All spin-polarized DFT computations were performed using the Vienna *ab initio* simulation package (VASP).[116,117] The Perdew–Burke–Ernzerhof (PBE) functional within the generalized gradient approximation (GGA) was utilized to describe the electron exchange–correlation interactions.[118] The pseudopotentials were described by the projector-augmented wave (PAW) method with a cutoff energy of 500 eV.[119] All atoms were fully relaxed until the energy and force reached the convergence tolerances of 1×10^{-5} eV and 0.02 eV $Å^{-1}$, respectively. The Monkhorst–Pack *k*-point mesh of $2 \times 2 \times 1$ was used to determine the Brillouin zone.[120] To prevent the periodic effect, an 18 Å vacuum space was created along the supercell's *z*-axis. The 5×5 supercell of graphene with 14.76 Å × 12.78 Å × 25 Å lattice parameters was modeled for calculations of 4O–Fe-Graph, 2N2O–Fe-Graph, O–2N2O–Fe-Graph and O–2N–2O–Fe–V-Graph as illustrated in SI Fig. 34. Bader charge analysis was employed to obtain a quantitative description of the charges in the Fe centers.[121]

Density functional theory (DFT) calculations were conducted to elucidate the mechanistic pathways for the conversion of H_2O_2 into O_2. We initially attempted to construct graphene models containing carboxylic acid functional groups at the edges and coordinated Fe centers with or without additional TMEDA ligands to reproduce the structural features of Fe:rGO and Fe(TMEDA):rGO. However, these large systems suffered from severe SCF instability, charge localization, and multiple local minima, leading to non-convergent results. Therefore, four simplified periodic models were established by substituting selected carbon atoms in graphene with nitrogen and/or oxygen atoms to reproduce the first-shell Fe–O/N coordination environment based on the EXAFS results (SI Fig. 34a). Specifically, the 4O–Fe-Graph model was designed to represent Fe:rGO after dissociation of two Fe-bound H_2O molecules, while O–2N2O–Fe-Graph, 2N2O–Fe-Graph, and O–2N2O–Fe–V-Graph were constructed to mimic Fe(TMEDA):rGO under different coordination environments: (i) after dissociation of one Fe-bound H_2O, (ii) after dissociation of one Fe-bound H_2O and one Fe-bound carboxylate, and (iii) after dissociation of one Fe-bound H_2O with an adjacent vacancy, respectively.

The proposed reaction pathway for conversion of H_2O_2 to O_2 is illustrated in SI Fig. 34b, and the corresponding energy profiles are presented in SI Fig. 34c. Initially, H_2O_2 adsorption occurred at the Fe centers with adsorption energies of −0.15 eV and −0.43 eV for the five-coordinate Fe sites in O–2N2O–Fe-Graph and O–2N2O–Fe–V-Graph, respectively. The adsorbed H_2O_2 subsequently dissociated into an adsorbed O atom and released H_2O, with relative energies of −1.33 eV and −0.74 eV for O–2N2O–Fe-Graph and O–2N2O–Fe–V-Graph, respectively. In contrast, no H_2O_2 adsorption was observed at the four-coordinate Fe sites in 4O–Fe-Graph and 2N2O-Graph. The adsorbed O species further reacted with another H_2O_2 molecule to generate adsorbed O_2 and released H_2O, with relative energies of −2.56, −2.19, −4.25, and −5.13 eV for O–2N2O–Fe-Graph, O–2N2O–Fe–V-Graph, 2N2O–Fe-Grap, and 4O–Fe-Graph, respectively. All reactions discussed above were exergonic, while the rate-determining step (RDS) was identified as the subsequent desorption of O_2 from the Fe center. The corresponding energy barriers for O_2 desorption were calculated to be 0.45, 0.08, 2.14, and 3.02 eV for O–2N2O–Fe-Graph, O–2N2O–Fe–V-Graph, 2N2O–Fe-Graph, and 4O–Fe-Graph, respectively. On the other hand, based on Bader charge analyses, the five-coordinate Fe centers exhibited higher positive charges (+1.53 e for O–2N2O–Fe-Graph and +1.68 e for O–2N2O–Fe–V-Graph) than the four-coordinate Fe centers (+1.20 e for 4O–Fe-Graph and +1.21 e for 2N2O–Fe-Graph). Despite the structural simplifications relative to Fe:rGO and Fe(TMEDA):rGO, these simplified models may provide valuable mechanistic insights into (a) the exothermic binding of H_2O_2 to the five-coordinate Fe centers in O–2N2O–Fe-Graph and O–2N2O–Fe–V-Graph, while no stable adsorption of H_2O_2 was found at the four-coordinate Fe centers in 4O–Fe-Graph and 2N2O-Graph, (b) the lower kinetic barriers for O_2 desorption from the five-coordinate Fe centers in O–2N2O–Fe-Graph and O–2N2O–Fe–V-Graph, as compared with those from the four-coordinate Fe centers in 4O–Fe-Graph and 2N2O-Graph, and (c) the crucial role of the electron-deficient Fe center in promoting H_2O_2 binding and activation.

Author contributions

These authors contributed equally: Dr Chieh-Wei Chung, Mr Jyun-Yau Huang, and Mr Jing-Guan Liang. C.-W. C. and T.-T. L. conceptualized the idea. C.-W. C. carried out the initial experiments. C.-W. C., J.-Y. H., J.-G. L., L. I., C.-C. C., and Y.-C. L. performed the experiments and data analysis. J.-L. C., T.-S. C., C.-L. C, and Y.-R. L supervised the XANES/EXAFS experiments. C.-C. H. supervised the oxygen evolution reaction experiments. H.-H. C. supervised the CV and electroconductivity experiments. Z.-H. L. supervised the magneto-voltaic experiments. M.-Y. L. supervised the HRTEM/HAADF-STEM experiments. U.-P. A. supervised the Mössbauer experiments. Y.-C. L. supervised the EPR experiments. C.-W. C. and T.-T. L. wrote the original draft. C.-W. C., L. I., U.-P. A., Y.-C. L., and T.-T. L. reviewed and edited the manuscript. Y.-C. C., U.-P. A., Y.-C. L., and T.-T. L. secured funding for the project. All authors have approved the final version of the manuscript.

Conflicts of interest

There are no conflicts to declare.

Data availability

The data supporting this article have been included as part of the supplementary information (SI). Supplementary information is available. See DOI: **https://doi.org/10.1039/d5sc05275k**.

© 2026 The Author(s). Published by the Royal Society of Chemistry

Open Access Article. Published on 03 November 2025. Downloaded on 4/1/2026 3:19:42 PM. This article is licensed under a Creative Commons Attribution-NonCommercial 3.0 Unported Licence.

Acknowledgements

We gratefully acknowledge the financial support from the National Science and Technology Council, Taiwan (NSTC 109-2628-M-007-003-MY3, NSTC 109-2622-M-007-003-CC2, NSTC 110-2622-M-007-002, NSTC 114-2218-E-007-012, NSTC 112-2628-M-007-004-MY4, NSTC 113-2218-E-007-014) and National Tsing Hua University, Taiwan (Grant No. 109Q2711E1 and 110Q2513E1). We thank the National Synchrotron Radiation Research Center (Taiwan) for the support with Fe K-edge XAS experiments; Mr Wen-Feng Chang (National Tsing Hua University) for the help with ICP-OES experiments; Mr Yung-Sheng Chen (National Tsing Hua University) for technical support with TEM, HRTEM, HAADF-STEM and corresponding EDS mapping manipulations; Ms. Ching-Wen Tsai (National Tsing Hua University) for the help with XPS measurements; Mr Bing-Heng Li (National Tsing Hua University) for the support with CV experiments; Ms. Ching-Wen Hwang (National Tsing Hua University) for the help with UV DRS measurements; and Ms. Juo-Chi Chen (National Tsing Hua University) and Dr Tzu-Hsien Tseng (National Chung Hsing University) for technical support with EPR measurements.

References

1 B. Qiao, A. Wang, X. Yang, L. F. Allard, Z. Jiang, Y. Cui, J. Liu, J. Li and T. Zhang, Single-atom Catalysis of CO Oxidation Using Pt_1/FeO_x, *Nat. Chem.*, 2011, **3**, 634–641.

2 H. L. Fei, J. C. Dong, Y. X. Feng, C. S. Allen, C. Z. Wan, B. Volosskiy, M. F. Li, Z. P. Zhao, Y. L. Wang, H. T. Sun, P. F. An, W. X. Chen, Z. Y. Guo, C. Lee, D. L. Chen, I. Shakir, M. J. Liu, T. D. Hu, Y. D. Li, A. I. Kirkland, X. F. Duan and Y. Huang, General Synthesis and Definitive Structural Identification of MN_4C_4 Single-atom Catalysts with Tunable Electrocatalytic Activities, *Nat. Catal.*, 2018, **1**, 63–72.

3 C. Peng, R. Pang, J. Li and E. Wang, Current Advances on the Single-Atom Nanozyme and its Bioapplications, *Adv. Mater.*, 2024, **36**, e2211724.

4 H. Jeong, S. Shin and H. Lee, Heterogeneous Atomic Catalysts Overcoming the Limitations of Single-Atom Catalysts, *ACS Nano*, 2020, **14**, 14355–14374.

5 X. L. Zhang, G. L. Li, G. Chen, D. Wu, X. X. Zhou and Y. N. Wu, Single-atom Nanozymes: A Rising Star for Biosensing and Biomedicine, *Coord. Chem. Rev.*, 2020, **418**, 213376.

6 Y. Liu, H. Zhao and Y. L. Zhao, Designing Efficient Single Metal Atom Biocatalysts at the Atomic Structure Level, *Angew. Chem., Int. Ed.*, 2024, **63**, e202315933.

7 M. Huo, L. Wang, Y. Wang, Y. Chen and J. Shi, Nanocatalytic Tumor Therapy by Single-Atom Catalysts, *ACS Nano*, 2019, **13**, 2643–2653.

8 X. Lu, L. Kuai, F. Huang, J. Jiang, J. Song, Y. Liu, S. Chen, L. Mao, W. Peng, Y. Luo, Y. Li, H. Dong, B. Li and J. Shi, Single-atom Catalysts-based Catalytic ROS Clearance for Efficient Psoriasis Treatment and Relapse Prevention *via* Restoring ESR1, *Nat. Commun.*, 2023, **14**, 6767.

9 L. Jiao, W. Xu, H. Yan, Y. Wu, C. Liu, D. Du, Y. Lin and C. Zhu, Fe-N-C Single-Atom Nanozymes for the Intracellular Hydrogen Peroxide Detection, *Anal. Chem.*, 2019, **91**, 11994–11999.

10 L. Huang, J. Chen, L. Gan, J. Wang and S. Dong, Single-atom Nanozymes, *Sci. Adv.*, 2019, **5**, eaav5490.

11 P. Peng, L. Shi, F. Huo, C. Mi, X. Wu, S. Zhang and Z. Xiang, A Pyrolysis-free Path toward Superiorly Catalytic Nitrogen-Coordinated Single Atom, *Sci. Adv.*, 2019, **5**, eaaw2322.

12 W. Wan, C. A. Triana, J. Lan, J. Li, C. S. Allen, Y. Zhao, M. Iannuzzi and G. R. Patzke, Bifunctional Single Atom Electrocatalysts: Coordination-Performance Correlations and Reaction Pathways, *ACS Nano*, 2020, **14**, 13279–13293.

13 D. Deng, X. Chen, L. Yu, X. Wu, Q. Liu, Y. Liu, H. Yang, H. Tian, Y. Hu, P. Du, R. Si, J. Wang, X. Cui, H. Li, J. Xiao, T. Xu, J. Deng, F. Yang, P. N. Duchesne, P. Zhang, J. Zhou, L. Sun, J. Li, X. Pan and X. Bao, A Single Iron Site Confined in a Graphene Matrix for the Catalytic Oxidation of Benzene at Room Temperature, *Sci. Adv.*, 2015, **1**, e1500462.

14 X. Cui, H. Li, Y. Wang, Y. Hu, L. Hua, H. Li, X. Han, Q. Liu, F. Yang, L. He, X. Chen, Q. Li, J. Xiao, D. Deng and X. Bao, Room-Temperature Methane Conversion by Graphene-Confined Single Iron Atoms, *Chem*, 2018, **4**, 1902–1910.

15 Y. Qu, L. Wang, Z. Li, P. Li, Q. Zhang, Y. Lin, F. Zhou, H. Wang, Z. Yang, Y. Hu, M. Zhu, X. Zhao, X. Han, C. Wang, Q. Xu, L. Gu, J. Luo, L. Zheng and Y. Wu, Ambient Synthesis of Single-Atom Catalysts from Bulk Metal *via* Trapping of Atoms by Surface Dangling Bonds, *Adv. Mater.*, 2019, **31**, 1904496.

16 Z. Wang and F. G. Wu, Emerging Single-Atom Catalysts/Nanozymes for Catalytic Biomedical Applications, *Adv. Healthc. Mater.*, 2022, **11**, e2101682.

17 F. F. Cao, L. Zhang, Y. W. You, L. R. Zheng, J. S. Ren and X. G. Qu, An Enzyme-Mimicking Single-Atom Catalyst as an Efficient Multiple Reactive Oxygen and Nitrogen Species Scavenger for Sepsis Management, *Angew. Chem., Int. Ed.*, 2020, **59**, 5108–5115.

18 Z. Guo, Y. Xie, J. Xiao, Z. J. Zhao, Y. Wang, Z. Xu, Y. Zhang, L. Yin, H. Cao and J. Gong, Single-Atom Mn-N_4 Site-Catalyzed Peroxone Reaction for the Efficient Production of Hydroxyl Radicals in an Acidic Solution, *J. Am. Chem. Soc.*, 2019, **141**, 12005–12010.

19 Y. Zhu, W. Sun, J. Luo, W. Chen, T. Cao, L. Zheng, J. Dong, J. Zhang, M. Zhang, Y. Han, C. Chen, Q. Peng, D. Wang and Y. Li, A Cocoon Silk Chemistry Strategy to Ultrathin N-doped Carbon Nanosheet with Metal Single-site Catalysts, *Nat. Commun.*, 2018, **9**, 3861.

20 W. Liu, L. L. Cao, W. R. Cheng, Y. J. Cao, X. K. Liu, W. Zhang, X. L. Mou, L. L. Jin, X. S. Zheng, W. Che, Q. H. Liu, T. Yao and S. Q. Wei, Single-Site Active Cobalt-Based Photocatalyst with a Long Carrier Lifetime for Spontaneous Overall Water Splitting, *Angew. Chem., Int. Ed.*, 2017, **56**, 9312–9317.

21 Y. Li, Z. S. Wu, P. Lu, X. Wang, W. Liu, Z. Liu, J. Ma, W. Ren, Z. Jiang and X. Bao, High-Valence Nickel Single-Atom Catalysts Coordinated to Oxygen Sites for Extraordinarily

Open Access Article. Published on 03 November 2025. Downloaded on 4/1/2026 3:19:42 PM. This article is licensed under a Creative Commons Attribution-NonCommercial 3.0 Unported Licence.

Activating Oxygen Evolution Reaction, *Adv. Sci.*, 2020, **7**, 1903089.

22 H. B. Yang, S. F. Hung, S. Liu, K. D. Yuan, S. Miao, L. P. Zhang, X. Huang, H. Y. Wang, W. Z. Cai, R. Chen, J. J. Gao, X. F. Yang, W. Chen, Y. Q. Huang, H. M. Chen, C. M. Li, T. Zhang and B. Liu, Atomically Dispersed Ni(I) as the Active Site for Electrochemical CO Reduction, *Nat. Energy*, 2018, **3**, 140–147.

23 H. T. Zhang, S. Y. Fang and Y. H. Hu, Recent Advances in Single-atom Catalysts for CO Oxidation, *Catal. Rev.*, 2022, **64**, 491–532.

24 H. Fei, J. Dong, M. J. Arellano-Jimenez, G. Ye, N. Dong Kim, E. L. Samuel, Z. Peng, Z. Zhu, F. Qin, J. Bao, M. J. Yacaman, P. M. Ajayan, D. Chen and J. M. Tour, Atomic Cobalt on Nitrogen-doped Graphene for Hydrogen Generation, *Nat. Commun.*, 2015, **6**, 8668.

25 H. Yang, B. Xu, S. Li, Q. Wu, M. Lu, A. Han and H. Liu, A Photoresponsive Nanozyme for Synergistic Catalytic Therapy and Dual Phototherapy, *Small*, 2021, **17**, 2007090.

26 H. Zhan, Z. Jiang, X. Luo, Y. Huang, D. Ye, W. Xu, C. Hu, H. Zhou, W. Lei and C. Yuan, A Versatile C/Fe_3O_4/C Self-Heating Electrode for Universal Application of Alternating Magnetic Fields in Electrocatalytic Hydrogen Production, *Adv. Funct. Mater.*, 2024, 2407600, DOI: **10.1002/adfm.202407600**.

27 X. Gong, Z. Jiang, W. Zeng, C. Hu, X. Luo, W. Lei and C. Yuan, Alternating Magnetic Field Induced Magnetic Heating in Ferromagnetic Cobalt Single-Atom Catalysts for Efficient Oxygen Evolution Reaction, *Nano Lett.*, 2022, **22**, 9411–9417.

28 D. Peng, C. Hu, X. Luo, J. Huang, Y. Ding, W. Zhou, H. Zhou, Y. Yang, T. Yu, W. Lei and C. Yuan, Electrochemical Reconstruction of NiFe/NiFeOOH Superparamagnetic Core/Catalytic Shell Heterostructure for Magnetic Heating Enhancement of Oxygen Evolution Reaction, *Small*, 2023, **19**, 2205665.

29 C. Niether, S. Faure, A. Bordet, J. Deseure, M. Chatenet, J. Carrey, B. Chaudret and A. Rouet, Improved Water Electrolysis using Magnetic Heating of FeC–Ni Core–shell Nanoparticles, *Nat. Energy*, 2018, **3**, 476–483.

30 H.-B. Zheng, Y.-L. Wang, P. Zhang, F. Ma, P.-Z. Gao, W.-M. Guo, H. Qin, X.-P. Liu and H.-N. Xiao, Multiple Effects Driven by AC Magnetic Field for Enhanced Electrocatalytic Oxygen Evolution in Alkaline Electrolyte, *Chem. Eng. J.*, 2021, **426**, 130785.

31 C.-W. Chung, B.-W. Liao, S.-W. Huang, S.-J. Chiou, C.-H. Chang, S.-J. Lin, B.-H. Chen, W.-L. Liu, S.-H. Hu, Y.-C. Chuang, C.-H. Lin, I.-J. Hsu, C.-M. Cheng, C.-C. Huang and T.-T. Lu, Magnetic Responsive Release of Nitric Oxide from an MOF-Derived Fe_3O_4@PLGA Microsphere for the Treatment of Bacteria-Infected Cutaneous Wound, *ACS Appl. Mater. Interfaces*, 2022, **14**, 6343–6357.

32 J.-G. Liang, W.-X. Gao, C.-W. Chung, L. A. Dayao, H.-H. Chou, Z.-H. Lin, D. Wan, J.-H. Huang, Y.-C. Chen and T.-T. Lu, Structure-dependent Magnetoelectric and Magnetothermal Effects of MOF-derived Zero-valence Cobalt and Iron Oxide Nanoparticles on a Carbonaceous Matrix, *Chem. Commun.*, 2024, **60**, 10136–10139.

33 J. Mazarío, S. Ghosh, V. Varela-Izquierdo, L. M. Martínez-Prieto and B. Chaudret, Magnetic Nanoparticles and Radio Frequency Induction: From Specific Heating to Magnetically Induced Catalysis, *ChemCatChem*, 2025, e202400683.

34 R. Zhang, X. Liu, N. Song, J. He, Z. Cen, C. Li, M. Wang, H. Tang, W. Liu, X. Ren and D. Ma, Magnetic Induction Heating-Driven Rapid Cold Start of Ammonia Decomposition for Hydrogen Production, *J. Am. Chem. Soc.*, 2024, **146**, 28635–28641.

35 Y. Zhang, C. Liang, J. Wu, H. Liu, B. Zhang, Z. Jiang, S. Li and P. Xu, Recent Advances in Magnetic Field-Enhanced Electrocatalysis, *ACS Appl. Energy Mater.*, 2020, **3**, 10303–10316.

36 G. H. El-Nowihy, M. M. Abdellatif and M. S. El-Deab, Magnetic Field-assisted Water Splitting at Ternary NiCoFe Magnetic Nanocatalysts: Optimization Study, *Renewable Energy*, 2024, **226**, 120395.

37 T. Wu and Z. J. Xu, Oxygen Evolution in Spin-sensitive Pathways, *Curr. Opin. Electrochem.*, 2021, **30**, 100804.

38 X. Ren, T. Wu, Y. Sun, Y. Li, G. Xian, X. Liu, C. Shen, J. Gracia, H.-J. Gao, H. Yang and Z. J. Xu, Spin-polarized Oxygen Evolution Reaction under Magnetic Field, *Nat. Commun.*, 2021, **12**, 2608.

39 Y. Sun, S. Sun, H. Yang, S. Xi, J. Gracia and Z. J. Xu, Spin-Related Electron Transfer and Orbital Interactions in Oxygen Electrocatalysis, *Adv. Mater.*, 2020, **32**, 2003297.

40 C.-Y. Huang, H.-A. Chen, W.-X. Lin, K.-H. Chen, Y.-C. Lin, T.-S. Wu, C.-C. Chang, C.-W. Pao, W.-T. Chuang, J.-C. Jan, Y.-C. Shao, N. Hiraoka, J.-W. Chiou, P.-C. Kuo, J. Shiue, D. V. S. K, R. Sankar, Z.-W. Cyue, W.-F. Pong and C.-W. Chen, In Situ Identification of Spin Magnetic Effect on Oxygen Evolution Reaction Unveiled by X-ray Emission Spectroscopy, *J. Am. Chem. Soc.*, 2025, **147**, 13286–13295.

41 M. K. Y. Kwok, C. C. J. Maley, A. Dworkin, S. Hattersley, P. Southern and Q. A. Pankhurst, Nonspecific Eddy Current Heating in Magnetic Field Hyperthermia, *Appl. Phys. Lett.*, 2023, **122**, 240502.

42 B. J. Moeller, R. A. Richardson and M. W. Dewhirst, Hypoxia and Radiotherapy: Opportunities for Improved Outcomes in Cancer Treatment, *Cancer Metastasis Rev.*, 2007, **26**, 241–248.

43 F. Pi, X. Deng, Q. Xue, L. Zheng, H. Liu, F. Yang and T. Chen, Alleviating the Hypoxic Tumor Microenvironment with MnO_2-coated CeO_2 Nanoplatform for Magnetic Resonance Imaging Guided Radiotherapy, *J. Nanobiotechnol.*, 2023, **21**, 90.

44 T. Lin, X. Zhao, S. Zhao, H. Yu, W. Cao, W. Chen, H. Wei and H. Guo, O_2-generating MnO_2 Nanoparticles for Enhanced Photodynamic Therapy of Bladder Cancer by Ameliorating Hypoxia, *Theranostics*, 2018, **8**, 990–1004.

45 R. Abou Khouzam, R. F. Zaarour, K. Brodaczewska, B. Azakir, G. H. Venkatesh, J. Thiery, S. Terry and S. Chouaib, The Effect of Hypoxia and Hypoxia-Associated

© 2026 The Author(s). Published by the Royal Society of Chemistry

Open Access Article. Published on 03 November 2025. Downloaded on 4/1/2026 3:19:42 PM. This article is licensed under a Creative Commons Attribution-NonCommercial 3.0 Unported Licence.

Pathways in the Regulation of Antitumor Response: Friends or Foes?, *Front. Immunol.*, 2022, **13**, 828875.

46 J. A. Bertout, S. A. Patel and M. C. Simon, The Impact of O_2 Availability on Human Cancer, *Nat. Rev. Cancer*, 2008, **8**, 967–975.

47 J. Ciepla and R. Smolarczyk, Tumor Hypoxia Unveiled: Insights into Microenvironment, Detection Tools and Emerging Therapies, *Clin. Exp. Med.*, 2024, **24**, 235.

48 Y. X. Zhang, J. H. Zhang, Q. Y. Jia, J. C. Ge and P. F. Wang, Innovative Strategies of Hydrogen Peroxide-involving Tumor Therapeutics, *Mater Chem Front*, 2021, **5**, 4474–4501.

49 C. Gorrini, I. S. Harris and T. W. Mak, Modulation of Oxidative Stress as an Anticancer Strategy, *Nat. Rev. Drug Discovery*, 2013, **12**, 931–947.

50 J. R. Stone and S. Yang, Hydrogen Peroxide: a Signaling Messenger, *Antioxid. Redox Signal.*, 2006, **8**, 243–270.

51 T. Ali, D. Li, T. N. F. Ponnamperumage, A. K. Peterson, J. Pandey, K. Fatima, J. Brzezinski, J. A. R. Jakusz, H. L. Gao, G. E. Koelsch, D. S. Murugan and X. H. Peng, Generation of Hydrogen Peroxide in Cancer Cells: Advancing Therapeutic Approaches for Cancer Treatment, *Cancers*, 2024, **16**, 2171.

52 G. Yang, L. Xu, Y. Chao, J. Xu, X. Sun, Y. Wu, R. Peng and Z. Liu, Hollow MnO_2 as a Tumor-microenvironment-responsive Biodegradable Nano-platform for Combination Therapy Favoring Antitumor Immune Responses, *Nat. Commun.*, 2017, **8**, 902.

53 C. R. Gordijo, A. Z. Abbasi, M. A. Amini, H. Y. Lip, A. Maeda, P. Cai, P. J. O'Brien, R. S. DaCosta, A. M. Rauth and X. Y. Wu, Design of Hybrid MnO_2-Polymer-Lipid Nanoparticles with Tunable Oxygen Generation Rates and Tumor Accumulation for Cancer Treatment, *Adv. Funct. Mater.*, 2015, **25**, 1858–1872.

54 C. Zhang, W. Bu, D. Ni, S. Zhang, Q. Li, Z. Yao, J. Zhang, H. Yao, Z. Wang and J. Shi, Synthesis of Iron Nanometallic Glasses and Their Application in Cancer Therapy by a Localized Fenton Reaction, *Angew. Chem., Int. Ed.*, 2016, **55**, 2101–2106.

55 Y. Liu, W. Zhen, Y. Wang, J. Liu, L. Jin, T. Zhang, S. Zhang, Y. Zhao, S. Song, C. Li, J. Zhu, Y. Yang and H. Zhang, One-Dimensional Fe_2P Acts as a Fenton Agent in Response to NIR II Light and Ultrasound for Deep Tumor Synergetic Theranostics, *Angew. Chem., Int. Ed.*, 2019, **58**, 2407–2412.

56 L. Wang, M. Huo, Y. Chen and J. Shi, Iron-engineered Mesoporous Silica Nanocatalyst with Biodegradable and Catalytic Framework for Tumor-specific Therapy, *Biomaterials*, 2018, **163**, 1–13.

57 Y. Su, F. Wu, Q. Song, M. Wu, M. Mohammadniaei, T. Zhang, B. Liu, S. Wu, M. Zhang, A. Li and J. Shen, Dual Enzyme-mimic Nanozyme based on Single-atom Construction Strategy for Photothermal-augmented Nanocatalytic Therapy in the Second Near-infrared Biowindow, *Biomaterials*, 2022, **281**, 121325.

58 L. Westwood, I. J. Nixon, E. Emmerson and A. Callanan, The Road after Cancer: Biomaterials and Tissue Engineering Approaches to Mediate the Tumor Microenvironment Post-cancer Treatment, *Front. Biomater. Sci.*, 2024, **3**, 1347324.

59 H. J. Jeon, H. J. Chun, H. S. Choi, B. Keum, H. B. Kim and J. H. Kim, Biphasic Regulation of Apoptosis Following Gastric Irreversible Electroporation Using Tissue Immunohistochemistry of Activated Caspase-3 with TUNEL Method, *Cancers*, 2024, **16**, 1389.

60 K.-C. Li, Z.-H. Wu, C.-H. Ke, Y.-C. Lee, J.-F. Lee, J.-M. Chen, S.-C. Haw, F.-T. Tsai and W.-F. Liaw, Selectivity and Activity Modulation of Electrocatalytic Carbon Dioxide Reduction by Atomically Dispersed Dual Iron Catalysts, *J. Mater. Chem. A*, 2023, **11**, 2377–2390.

61 L. Que, *Physical Methods in Bioinorganic Chemistry : Spectroscopy and Magnetism*, University Science Books, Sausalito, Calif., 2000.

62 E. S. Orth, J. G. L. Ferreira, J. E. S. Fonsaca, S. F. Blaskievicz, S. H. Domingues, A. Dasgupta, M. Terrones and A. J. G. Zarbin, pKa Determination of Graphene-like Materials: Validating Chemical Functionalization, *J. Colloid Interface Sci.*, 2016, **467**, 239–244.

63 V. L. E. Siong, X. H. Tai, K. M. Lee, J. C. Juan and C. W. Lai, Unveiling the Enhanced Photoelectrochemical and Photocatalytic Properties of Reduced Graphene Oxide for Photodegradation of Methylene Blue Dye, *RSC Adv.*, 2020, **10**, 37905–37915.

64 M. T. Dejpasand, E. Saievar-Iranizad, A. Bayat, A. Montaghemi and S. R. Ardekani, Tuning HOMO and LUMO of Three Region (UV, Vis and IR) Photoluminescent Nitrogen Doped Graphene Quantum Dots for Photodegradation of Methylene Blue, *Mater. Res. Bull.*, 2020, **128**, 110886.

65 S. C. Perry, D. Pangotra, L. Vieira, L. I. Csepei, V. Sieber, L. Wang, C. P. de León and F. C. Walsh, Electrochemical Synthesis of Hydrogen Peroxide from Water and Oxygen, *Nat. Rev. Chem.*, 2019, **3**, 442–458.

66 S. Zhang, Y. Li, S. Sun, L. Liu, X. Mu, S. Liu, M. Jiao, X. Chen, K. Chen, H. Ma, T. Li, X. Liu, H. Wang, J. Zhang, J. Yang and X. D. Zhang, Single-atom Nanozymes Catalytically Surpassing Naturally Occurring Enzymes as Sustained Stitching for Brain Trauma, *Nat. Commun.*, 2022, **13**, 4744.

67 H. J. Forman and H. Zhang, Targeting Oxidative Stress in Disease: Promise and Limitations of Antioxidant Therapy, *Nat. Rev. Drug Discovery*, 2021, **20**, 689–709.

68 F. Wu, Y. Du, J. Yang, B. Shao, Z. Mi, Y. Yao, Y. Cui, F. He, Y. Zhang and P. Yang, Peroxidase-like Active Nanomedicine with Dual Glutathione Depletion Property to Restore Oxaliplatin Chemosensitivity and Promote Programmed Cell Death, *ACS Nano*, 2022, **16**, 3647–3663.

69 Z. Li and J. Cui, Targeting the Lactic Acid Metabolic Pathway for Antitumor Therapy, *Mol. Ther. Oncolytics*, 2023, **31**, 100740.

70 S. Meyer, I. Klawitter, S. Demeshko, E. Bill and F. Meyer, A Tetracarbene–Oxoiron(IV) Complex, *Angew. Chem., Int. Ed.*, 2013, **52**, 901–905.

71 M. Puri and L. Que, Jr., Toward the Synthesis of More Reactive S = 2 Non-Heme Oxoiron(IV) Complexes, *Acc. Chem. Res.*, 2015, **48**, 2443–2452.

Open Access Article. Published on 03 November 2025. Downloaded on 4/1/2026 3:19:42 PM. This article is licensed under a Creative Commons Attribution-NonCommercial 3.0 Unported Licence.

72 M. A. Ehudin, L. B. Gee, S. Sabuncu, A. Braun, P. Moënne-Loccoz, B. Hedman, K. O. Hodgson, E. I. Solomon and K. D. Karlin, Tuning the Geometric and Electronic Structure of Synthetic High-Valent Heme Iron(IV)-Oxo Models in the Presence of a Lewis Acid and Various Axial Ligands, *J. Am. Chem. Soc.*, 2019, **141**, 5942–5960.

73 D. Santhanaraj, A. Selvamani, K. Rajakumar, N. R. Joseph, S. Giridhar, T. Adinaveen, P. L. Sophie and V. Ramkumar, Unravelling the Cooperative Role of Lattice Strain on MnO_2/TiO_2 and MnO_2/ZnO Catalysts for the Fast Decomposition of Hydrogen Peroxide, *New J. Chem.*, 2021, **45**, 9944–9958.

74 S. Özcan, Ç. Z. Süngü Akdoğan, M. Polat, Ç. Kip and A. Tuncel, A New Multimodal Magnetic Nanozyme and a Reusable Peroxymonosulfate Oxidation Catalyst: Manganese Oxide Coated-Monodisperse-porous and Magnetic Core-shell Microspheres, *Chemosphere*, 2023, **341**, 140034.

75 W. Zhu, Z. Dong, T. Fu, J. Liu, Q. Chen, Y. Li, R. Zhu, L. Xu and Z. Liu, Modulation of Hypoxia in Solid Tumor Microenvironment with MnO_2 Nanoparticles to Enhance Photodynamic Therapy, *Adv. Funct. Mater.*, 2016, **26**, 5490–5498.

76 W. Ma, J. Mao, X. Yang, C. Pan, W. Chen, M. Wang, P. Yu, L. Mao and Y. Li, A Single-atom Fe–N4 Catalytic Site Mimicking Bifunctional Antioxidative Enzymes for Oxidative Stress Cytoprotection, *Chem. Comm.*, 2019, **55**, 159–162.

77 R. Zhang, B. Xue, Y. Tao, H. Zhao, Z. Zhang, X. Wang, X. Zhou, B. Jiang, Z. Yang, X. Yan and K. Fan, Edge-Site Engineering of Defective Fe–N4 Nanozymes with Boosted Catalase-Like Performance for Retinal Vasculopathies, *Adv. Mater.*, 2022, **34**, 2205324.

78 S. Zhang, Y. Li, S. Sun, L. Liu, X. Mu, S. Liu, M. Jiao, X. Chen, K. Chen, H. Ma, T. Li, X. Liu, H. Wang, J. Zhang, J. Yang and X.-D. Zhang, Single-atom Nanozymes Catalytically Surpassing Naturally Occurring Enzymes as Sustained Stitching for Brain Trauma, *Nat. Commun.*, 2022, **13**, 4744.

79 T. E. Westre, P. Kennepohl, J. G. DeWitt, B. Hedman, K. O. Hodgson and E. I. Solomon, A Multiplet Analysis of Fe K-Edge 1s → 3d Pre-Edge Features of Iron Complexes, *J. Am. Chem. Soc.*, 1997, **119**, 6297–6314.

80 C. Zhao, C. Xiong, X. Liu, M. Qiao, Z. Li, T. Yuan, J. Wang, Y. Qu, X. Wang, F. Zhou, Q. Xu, S. Wang, M. Chen, W. Wang, Y. Li, T. Yao, Y. Wu and Y. Li, Unraveling the Enzyme-like Activity of Heterogeneous Single Atom Catalyst, *Chem. Commun.*, 2019, **55**, 2285–2288.

81 S. Chen, S. Guan, J. Tan, W. Lu, H. Zhang, J. Qiu, H. Zhu and X. Liu, Electron-Deficient Effect Modulates Catalase-Like Activity of Iron-Nitrogen-Carbon Nanozymes for Inflammatory Wound Therapy, *Adv. Funct. Mater.*, 2024, **34**, 2411202.

82 T. A. Jackson, J.-U. Rohde, M. S. Seo, C. V. Sastri, R. DeHont, A. Stubna, T. Ohta, T. Kitagawa, E. Münck, W. Nam and L. Que, Jr., Axial Ligand Effects on the Geometric and Electronic Structures of Nonheme Oxoiron(IV) Complexes, *J. Am. Chem. Soc.*, 2008, **130**, 12394–12407.

83 J. England, M. Martinho, E. R. Farquhar, J. R. Frisch, E. L. Bominaar, E. Münck and L. Que Jr., A Synthetic High-Spin Oxoiron(IV) Complex: Generation, Spectroscopic Characterization, and Reactivity, *Angew. Chem., Int. Ed.*, 2009, **48**, 3622–3626.

84 D. C. Lacy, R. Gupta, K. L. Stone, J. Greaves, J. W. Ziller, M. P. Hendrich and A. S. Borovik, Formation, Structure, and EPR Detection of a High Spin Fe^{IV}—Oxo Species Derived from Either an Fe^{III}—Oxo or Fe^{III}—OH Complex, *J. Am. Chem. Soc.*, 2010, **132**, 12188–12190.

85 V. F. Oswald, J. L. Lee, S. Biswas, A. C. Weitz, K. Mittra, R. Fan, J. Li, J. Zhao, M. Y. Hu, E. E. Alp, E. L. Bominaar, Y. Guo, M. T. Green, M. P. Hendrich and A. S. Borovik, Effects of Noncovalent Interactions on High-Spin Fe(IV)–Oxido Complexes, *J. Am. Chem. Soc.*, 2020, **142**, 11804–11817.

86 J. Krzystek, J. England, K. Ray, A. Ozarowski, D. Smirnov, L. Que, Jr. and J. Telser, Determination by High-Frequency and -Field EPR of Zero-Field Splitting in Iron(IV) Oxo Complexes: Implications for Intermediates in Nonheme Iron Enzymes, *Inorg. Chem.*, 2008, **47**, 3483–3485.

87 J.-U. Rohde, S. Torelli, X. Shan, M. H. Lim, E. J. Klinker, J. Kaizer, K. Chen, W. Nam and L. Que, Structural Insights into Nonheme Alkylperoxoiron(III) and Oxoiron(IV) Intermediates by X-ray Absorption Spectroscopy, *J. Am. Chem. Soc.*, 2004, **126**, 16750–16761.

88 J. P. Bigi, W. H. Harman, B. Lassalle-Kaiser, D. M. Robles, T. A. Stich, J. Yano, R. D. Britt and C. J. Chang, A High-Spin Iron(IV)–Oxo Complex Supported by a Trigonal Nonheme Pyrrolide Platform, *J. Am. Chem. Soc.*, 2012, **134**, 1536–1542.

89 R. Gupta, D. C. Lacy, E. L. Bominaar, A. S. Borovik and M. P. Hendrich, Electron Paramagnetic Resonance and Mössbauer Spectroscopy and Density Functional Theory Analysis of a High-Spin FeIV–Oxo Complex, *J. Am. Chem. Soc.*, 2012, **134**, 9775–9784.

90 A. Y. Satoh, J. E. Trosko and S. J. Masten, Methylene Blue Dye Test for Rapid Qualitative Detection of Hydroxyl Radicals Formed in a Fenton's Reaction Aqueous Solution, *Environ. Sci. Technol.*, 2007, **41**, 2881–2887.

91 Q. Sun, K. Wu, J. Zhang and J. Sheng, Construction of $ZnFe_2O_4$/rGO Composites as Selective Magnetically Recyclable Photocatalysts under Visible Light Irradiation, *Nanotechnology*, 2019, **30**, 315706.

92 Y.-C. Chan, Y.-H. Lin, H.-C. Liu, R.-S. Hsu, M.-R. Chiang, L.-W. Wang, T.-C. Chou, T.-T. Lu, I. C. Lee, L.-A. Chu and S.-H. Hu, *In situ* Magnetoelectric Generation of Nitric Oxide and Electric Stimulus for Nerve Therapy by Wireless Chargeable Molybdenum Carbide Octahedrons, *Nano Today*, 2023, **51**, 101935.

93 R.-S. Hsu, S.-J. Li, J.-H. Fang, I. C. Lee, L.-A. Chu, Y.-C. Lo, Y.-J. Lu, Y.-Y. Chen and S.-H. Hu, Wireless Charging-mediated Angiogenesis and Nerve Repair by Adaptable Microporous Hydrogels from Conductive Building Blocks, *Nat. Commun.*, 2022, **13**, 5172.

94 S.-L. Cho, C.-J. Liao and T.-T. Lu, Synthetic Methodology for Preparation of Dinitrosyl Iron Complexes, *J. Biol. Inorg. Chem.*, 2019, **24**, 495–515.

© 2026 The Author(s). Published by the Royal Society of Chemistry

Open Access Article. Published on 03 November 2025. Downloaded on 4/1/2026 3:19:42 PM. This article is licensed under a Creative Commons Attribution-NonCommercial 3.0 Unported Licence.

95 H.-C. Huang, W.-M. Ching, Y.-T. Tseng, C.-H. Chen and T.-T. Lu, Transformation of the Hydride-containing Dinitrosyl Iron Complex $[(NO)_2Fe(\eta^2\text{-}BH_4)]^-$ into $[(NO)_2Fe(\eta^3\text{-}HCS_2)]^-$ *via* Reaction with CS_2, *Dalton Trans.*, 2019, **48**, 5897–5902.

96 M.-C. Hung, M.-C. Tsai, G.-H. Lee and W.-F. Liaw, Transformation and Structural Discrimination between the Neutral $\{Fe(NO)_2\}^{10}$ Dinitrosyliron Complexes (DNICs) and the Anionic/Cationic $\{Fe(NO)_2\}^9$ DNICs, *Inorg. Chem.*, 2006, **45**, 6041–6047.

97 I. Prisecaru, *WMOSS4 Mössbauer Spectral Analysis Software*, **https://www.wmoss.org**, 2009-2016.

98 W. S. Hummers Jr and R. E. Offeman, Preparation of Graphitic Oxide, *J. Am. Chem. Soc.*, 1958, **80**, 1339.

99 N. K. Sudesh, S. Das, C. Bernhard and G. D. Varma, Effect of Graphene Oxide Doping on Superconducting Properties of Bulk MgB_2, *Supercond. Sci. Technol.*, 2013, **26**, 095008.

100 A. Omidvar, M. R. RashidianVaziri, B. Jaleh, N. Partovi Shabestari and M. Noroozi, Metal-enhanced Fluorescence of Graphene Oxide by Palladium Nanoparticles in the Blue–green Part of the Spectrum, *Chin. Phys. B*, 2016, **25**, 118102.

101 I. O. Faniyi, O. Fasakin, B. Olofinjana, A. S. Adekunle, T. V. Oluwasusi, M. A. Eleruja and E. O. B. Ajayi, The Comparative Analyses of Reduced Graphene Oxide (RGO) Prepared *via* Green, Mild and Chemical Approaches, *SN Appl. Sci.*, 2019, **1**, 1181.

102 V. G. Sreeja, G. Vinitha, R. Reshmi, E. I. Anila and M. K. Jayaraj, Effect of Reduction Time on Third Order Optical Nonlinearity of Reduced Graphene Oxide, *Opt. Mater.*, 2017, **66**, 460–468.

103 R. Al-Gaashani, A. Najjar, Y. Zakaria, S. Mansour and M. A. Atieh, XPS and Structural Studies of High Quality Graphene Oxide and Reduced Graphene Oxide Prepared by Different Chemical Oxidation Methods, *Ceram. Int.*, 2019, **45**, 14439–14448.

104 S.-D. Jiang, Z.-M. Bai, G. Tang, Y. Hu and L. Song, Fabrication and Characterization of Graphene oxide-reinforced Poly(vinyl alcohol)-based Hybrid Composites by the Sol–gel Method, *Compos. Sci. Technol.*, 2014, **102**, 51–58.

105 J. R. Rani, J. Lim, J. Oh, D. Kim, D. Lee, J.-W. Kim, H. S. Shin, J. H. Kim and S. C. Jun, Substrate and Buffer Layer Effect on the Structural and Optical Properties of Graphene Oxide Thin Films, *RSC Adv.*, 2013, **3**, 5926–5936.

106 P. Li, Y. Xuan, B. Jiang, S. Zhang and C. Xia, Hollow $La_{0.6}Sr_{0.4}Ni_{0.2}Fe_{0.75}Mo_{0.05}O_{3-\delta}$ Electrodes with Exsolved $FeNi_3$ in Quasi-symmetrical Solid Oxide Electrolysis Cells for Direct CO_2 Electrolysis, *Electrochem. Commun.*, 2022, **134**, 107188.

107 K. L. Ai, Y. L. Liu, L. H. Lu, X. L. Cheng and L. H. Huo, A Novel Strategy for Making Soluble Reduced Graphene Oxide Sheets Cheaply by Adopting an Endogenous Reducing Agent, *J. Mater. Chem.*, 2011, **21**, 3365–3370.

108 X.-Z. Tang, N. Srikanth, X.-Q. Feng, C. K. Chua and K. Zhou, Reduced Graphene Oxide/Silver Hybrid with N,N-Dimethyl Formamide for Oxygen Reduction Reactions and Surface Enhanced Raman Scattering, *RSC Adv.*, 2016, **6**, 102519–102527.

109 R. Tarcan, M. Handrea-Dragan, O. Todor-Boer, I. Petrovai, C. Farcau, M. Rusu, A. Vulpoi, M. Todea, S. Astilean and I. Botiz, A New, Fast and Facile Synthesis Method for Reduced Graphene Oxide in N, N-Dimethylformamide, *Synth. Met.*, 2020, **269**, 116576.

110 S. Seo, Y. Yoon, J. Lee, Y. Park and H. Lee, Nitrogen-doped Partially Reduced Graphene Oxide Rewritable Nonvolatile Memory, *ACS Nano*, 2013, **7**, 3607–3615.

111 K. Ai, Y. Liu, L. Lu, X. Cheng and L. Huo, A Novel Strategy for Making Soluble Reduced Graphene Oxide Sheets Cheaply by Adopting an Endogenous Reducing Agent, *J. Mater. Chem.*, 2011, **21**, 3365–3370.

112 S. Kim, K. Choi and S. Park, Solvothermal Reduction of Graphene Oxide in Dimethylformamide, *Solid State Sci.*, 2016, **61**, 40–43.

113 A. Zhou, L. Li, M. Li and Q. Chen, Fabrication of Poly(amide-co-ester) Solvent Resistant Nanofiltration Membrane from P-nitrophenol and Trimethyl Chloride *via* Interfacial Polymerization, *Separations*, 2022, **9**, 28.

114 W. M. Silva, H. Ribeiro, L. M. Seara, H. D. R. Calado, A. S. Ferlauto, R. M. Paniago, C. F. Leite and G. G. Silva, Surface Properties of Oxidized and Aminated Multi-Walled Carbon Nanotubes, *J Brazil Chem Soc*, 2012, **23**, 1078–1086.

115 S. G. Rhee, T. S. Chang, W. Jeong and D. Kang, Methods for Detection and Measurement of Hydrogen Peroxide Inside and Outside of Cells, *Mol. Cells*, 2010, **29**, 539–549.

116 J. Hafner, Ab-initio Simulations of Materials using VASP: Density-functional Theory and Beyond, *J. Comput. Chem.*, 2008, **29**, 2044–2078.

117 G. Sun, J. Kürti, P. Rajczy, M. Kertesz, J. Hafner and G. Kresse, Performance of the Vienna *ab initio* Simulation Package (VASP) in Chemical Applications, *J. Mol. Struct. THEOCHEM*, 2003, **624**, 37–45.

118 J. P. Perdew, K. Burke and M. Ernzerhof, Generalized Gradient Approximation Made Simple, *Phys. Rev. Lett.*, 1996, **77**, 3865–3868.

119 P. E. Blöchl, Projector Augmented-wave Method, *Phys. Rev. B*, 1994, **50**, 17953–17979.

120 H. J. Monkhorst and J. D. Pack, Special Points for Brillouin-zone Integrations, *Phys. Rev. B*, 1976, **13**, 5188–5192.

121 W. Tang, E. Sanville and G. Henkelman, A Grid-based Bader Analysis Algorithm without Lattice Bias, *J. Phys. Condens. Matter*, 2009, **21**, 084204.

© 2026 The Author(s). Published by the Royal Society of Chemistry